Journal of Materials Chemistry C

ROYAL SOCIETY OF CHEMISTRY

REVIEW

View Article Online
View Journal | View Issue

Cite this: J. Mater. Chem. C, 2023, 11, 10121

A comprehensive review of gallium nitride (GaN)-based gas sensors and their dynamic responses

Yang Jiang, [abc] Wenmao Li, [b] Fangzhou Du, [b] Robert Sokolovskij, [b] Yi Zhang, [abc] Shuhui Shi, [abc] Weiguo Huang, [d] Qing Wang, *[b] Hongyu Yu *[b] and Zhongrui Wang *[ac]

Received 30th March 2023,
Accepted 20th June 2023

DOI: 10.1039/d3tc01126g

rsc.li/materials-c

Gas-sensing technology that is ubiquitous has progressively gained significance in our daily lives. There is a growing requirement for real-time, dependable and low-concentration gas detection to monitor toxic and flammable gases in industrial facilities, guarantee environmental air quality, identify automotive exhaust emissions, perform breath analysis for the early detection of diseases and so on. The appeal for gallium nitride (GaN)-based gas sensors has surged due to their chemical and temperature stability, making them suitable for deployment under harsh demanding conditions. The dynamic characteristics of GaN-based gas sensors reflect the absorption/desorption kinetics of molecules, and play a crucial role in determining their sensing performance, efficiency, and subsequent signal processing. This paper provides a comprehensive review of recent advancements in GaN-based gas sensors, with a focus on their dynamic response-related behaviors. The following key aspects are covered: First, we present an overview of the representative device structures of GaN-based gas sensors and highlight their figures of merits. Second, we examine the various techniques employed in the fabrication of these sensors. Third, we delve into the dipole-based sensing mechanism, the thermodynamic model governing gas absorption and desorption processes, and explore the relationship between response and recovery times with temperature and concentration. Fourth, we explore the practical applications of the gas sensors' dynamic responses. Finally, we analyze the impact of device structure design on the dynamic responses of GaN-based gas sensors, along with post-signal processing methods.

[a] Department of Electrical and Electronic Engineering, The University of Hong Kong, Pokfulam Road, Hong Kong. E-mail: zrwang@eee.hku.hk
[b] School of Microelectronics, Southern University of Science and Technology, Shenzhen, 518055, China. E-mail: wangq7@sustech.edu.cn, yuhy@sustech.edu.cn
[c] ACCESS – AI Chip Center for Emerging Smart Systems, InnoHK Centers, Hong Kong Science Park, Hong Kong
[d] Fujian Institute of Research on the Structure of Matter, Chinese Academy of Sciences, Fuzhou, 350002, China

Yang Jiang

Mr Yang Jiang received his BEng in microelectronic technology from Southern University of Science and Technology (SUSTech). He is currently pursuing his PhD degree at the Department of Electrical and Electronic Engineering, The University of Hong Kong. His research interests include GaN-based semiconductor materials and devices, emerging memristors and in-memory/sensor computing.

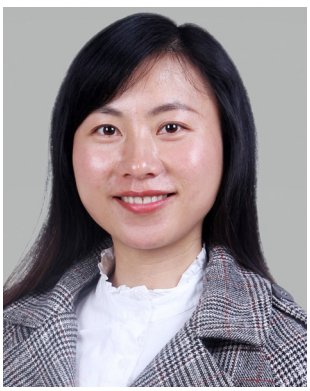

Qing Wang

Dr Qing Wang is a research associate professor and doctoral supervisor of the School of Microelectronics at Southern University of Science and Technology (SUSTech). She received her master's and doctoral degree from South China University of Technology. She did her post-doctoral research at Sun Yat-Sen University. Her main research focuses on the structure design and fabrication of GaN power and RF devices for 5G communication, smart power grid and new energy vehicles application.

1. Introduction

In recent years, there has been a notable surge of interest in semiconductor-type gas sensors, primarily due to their immense potential and notable advantages, including (1) high sensitivity of detection, (2) a wide range of operating temperatures, (3) short response time, (4) reproducibility, (5) scalable device size, and (6) low cost and power consumption. The aforementioned properties make semiconductor-type gas sensors highly promising for research and application in various areas, such as monitoring air quality, measuring pollutants in automotive exhaust emissions, detecting leakages in industrial processes, and for breath analysis.[1–4] Conventional gas sensors based on silicon (Si) field-effect transistors (FETs) have gained popularity due to their well-established fabrication techniques and affordability. However, the operational limitations of these sensors arise from their narrow bandgap (1.12 eV) and the inadequate chemical stability of Si, preventing them from functioning above 200 °C and in harsh environments. Beyond this temperature threshold, the elevated intrinsic carrier concentration significantly increases the risk of leakage current flowing into the substrate, ultimately posing a potential hazard of device failure.[5] Contrarily, a higher operating temperature exceeding 250 °C can greatly enhance the sensitivity of most semiconductor-type sensors.[6] Consequently, there is an increasing need for semiconductor materials possessing larger bandgaps (>2 eV) to overcome the limitations associated with conventional Si-based gas sensors.

Wide-bandgap (WBG) semiconductors are those having a bandgap larger than 2 eV. Several materials such as silicon carbide (SiC), diamond, gallium oxide (Ga_2O_3), and gallium nitride (GaN) have been widely studied for various FET applications. Among these materials, GaN shows significant promise for next-generation power electronics, radio-frequency and optoelectronic devices owing to its low cost and ease of fabrication.[7–9] In addition, GaN possesses notable advantages such as high chemical stability, thermal resistance, corrosion resistance and a weak Fermi-level pinning effect, enabling it to surpass the limitations commonly associated with Si-based devices.[10–16] Therefore, GaN-based devices have demonstrated tremendous potential for gas detection applications.[17,18]

Conventional GaN-based devices employ AlGaN/GaN heterojunction structure. This structure induces spontaneous and piezoelectric polarization effects between AlGaN and GaN, leading to the formation of a two-dimensional electron gas (2-DEG) at the interface. As a result, the gas sensing capabilities of these devices are significantly enhanced. The high carrier density of 2-DEG enables it to be highly responsive to subtle changes in the surrounding ambient conditions, contributing to their exceptional gas sensing capabilities.[19–21] Moreover, the high carrier mobility (>1500 cm^2 V^{-1} s^{-1}) and saturation electron velocity (2.5×10^7 cm s^{-1}) enable rapid movement of charge carriers, resulting in faster sensing and detection capabilities in GaN-based devices.[22–24] As a result, GaN-based devices offer significant advantages for high-speed, low-concentration, and highly reliable gas sensors. These devices exhibit larger sensing currents and high signal-to-noise ratios (SNRs), making them well-suited for sensitive and accurate gas detection. GaN-based sensors are typically fabricated on sapphire or silicon (Si) substrates, which are compatible with mature, cost-effective, and large complementary metal–oxide–semiconductor (CMOS) wafer fabrication techniques. This compatibility enables the monolithic integration of GaN-based sensors with other Si-based electronic devices, paving the way for advanced applications and improved functionality.[25,26]

To assess the gas-sensing performance of GaN-based sensors, various parameters such as response sensitivity (S_R), limit of detection (LOD), response time (τ_a), and recovery time (τ_b) have been proposed. These parameters provide valuable insights into the performance characteristics of GaN-based sensors, enabling the evaluation and comparison of their gas-sensing capabilities. The values of τ_a and τ_b reflect the dynamic response characteristics of the sensors when the target gas is introduced and subsequently removed. They are the most critical parameters that reveal the speed and efficiency of the sensor's response to changes in gas concentration. The demand for

Hongyu Yu

Dr Hongyu Yu is currently serving as a professor and Dean of School of Microelectronics, Southern University of Science and Technology (SUSTech). He received BEng from Tsinghua University, MSci from the University of Toronto and PhD from National University of Singapore. His main research areas include CMOS, novel ultra-high density memory, GaN device and system integration, and electronic ceramics.

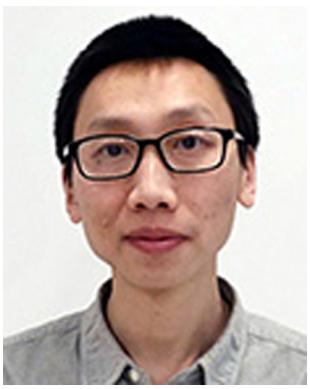

Zhongrui Wang

Dr Zhongrui Wang is an assistant professor at the Department of Electrical and Electronic Engineering at the University of Hong Kong. Prior to joining HKU, he received both BEng (first-class honour) and PhD from Nanyang Technological University in Singapore. He did his post-doctoral research at the University of Massachusetts Amherst. His research interest lies in emerging memory based neuromorphic computing and machine learning.

sensing devices that offer high-speed response has become increasingly urgent in order to meet the ever-growing requirements of real-time gas monitoring. However, the dynamic response of GaN-based gas sensors, specifically the temporal response of source–drain currents in relation to the temporal changes in gas concentration and temperature, has not been extensively explored or surveyed in the existing literature. The temporal responses of GaN-based gas sensors not only provide insights into the underlying mechanisms of gas molecule absorption and desorption processes but also assist in identifying the optimal balance between sensing throughput and sensing energy. Furthermore, the dynamic responses of GaN-based gas sensors involve in-sensor signal processing, which offers advantages in terms of footprint and system complexity. This is particularly significant in the context of smart systems in the era of the Internet of Things (IoT). This gap highlights the importance of conducting a review to investigate the temporal response of GaN-based gas sensors for a comprehensive understanding of their performance.

Several experimental studies have been conducted to benchmark and profile the temporal responses of GaN-based gas sensors. These studies aim to characterize and analyze the dynamic behavior of the sensors at different gas concentrations, temperatures, and operating parameters.[27–30] The observations regarding the dynamic responses of GaN-based gas sensors are supported by several theoretical formulations. These theoretical models aim to explain the impact of temperature and gas concentration on the dynamic behavior of the sensors.[31–36] This review serves as a comprehensive integration of the important research conducted in GaN-based gas sensors, consolidating and summarizing both the relevant experimental findings and theoretical work. In this review, we focus on representative studies that have investigated GaN-based gas sensors for the detection of various gases. We examine the key figures of merit associated with these sensors, such as sensitivity, selectivity, and detection limits. Additionally, we specifically emphasize the dynamic response-related behaviors of GaN-based gas sensors. The remaining sections of this paper are organized as follows: Section 2 explores the three main device structures commonly used for GaN-based gas sensors. It provides a comprehensive overview of these structures and summarizes the key parameters used to evaluate the sensing performance of GaN-based gas sensors. Section 3 gives a brief introduction of the various techniques and fabrication processes employed for GaN-based gas sensors. Section 4 presents the dipole-induced sensing mechanism and thermodynamic model to explain the gas absorption and desorption processes, along with an examination of the factors influencing the response and recovery times, such as temperature and gas concentration. Section 5 focuses on the significance of the dynamic responses of GaN-based sensors in the application of electronic noses (E-noses) and artificial olfactory systems (AOS). Section 6 considers the influence of device structure design on the dynamic responses and assesses of the future prospects of GaN-based gas sensors based on their performance, dynamic mechanism, and potential applications.

2. Types of GaN-based gas sensors

GaN-related materials have been utilized to fabricate different sensor structures, including metal–oxide semiconductor (MOS) diodes and transistors, Schottky diodes, and high-electron-mobility transistors (HEMTs). These structures have been employed to develop gas sensors for various gases such as hydrogen (H_2), hydrogen sulfide (H_2S), ammonia (NH_3), nitrogen oxide (NO_x), and carbon oxide (CO_x). The first GaN-based Schottky diode was demonstrated by Luther *et al.* using a Pt anode. The device exhibited sensing responses to hydrogen (H_2) and propane (C_3H_8) in the temperature range of 200–400 °C.[37] The values of LOD of H_2 and C_3H_8 were 2.5 ppm at 200 °C and 1000 ppm at 400 °C. The device demonstrated no degradation in its sensing characteristics even after being exposed to an argon (Ar) and oxygen (O_2) ambient for 500 hours at 400 °C. The first AlGaN/GaN heterostructure-based HEMT sensor was demonstrated by Schalwig *et al.* using a Pt gate.[38] The capability of the sensors to detect H_2, C_2H_4, and CO was tested at 300 °C, and a significant response current increase was observed for H_2, while the response current for C_2H_4 and CO was lower at the same concentration. MOS-based Schottky diode on the AlGaN/GaN heterostructure was first introduced by Kang *et al.* by using Sc_2O_3 as an insulator with a Pt anode.[39] The response to 10% H_2 in N_2 was observed. The same group also demonstrated an MOS-HEMT with an Sc_2O_3 gate dielectric and Pt metal to sense H_2 at room temperature, and a significant increase in the response current was reported.[40]

2.1. Schottky diode sensors

GaN-based Schottky diode-type devices offer the advantage of chemical stability due to their inherent characteristics, including a wide bandgap and a high exciton binding energy. Additionally, Schottky diode-type sensors feature (1) bidirectional response, (2) a wide range of operating temperatures, (3) a high sensing response, and (4) a small size.[41]

GaN-based Schottky diode sensors exhibit the forward and reverse current changes when exposed to the target gas due to variations in Schottky barrier height Φ_B, even at a high temperature. The thermionic emission transport mechanism dictates that when the applied forward voltage is $V > 3k_BT/q$, the I–V characteristics of Schottky diodes can be described using the following equations:[41,42]

$$I_F = I_s\left[\left(\frac{qV}{nk_BT}\right) - 1\right] \quad (1)$$

$$I_S = AA^*T^2\exp\left(-\frac{q\Phi_B}{k_BT}\right) \quad (2)$$

where I_F is the forward current and I_S is the reverse saturation current. T, A, A^*, Φ_B, q, k_B, and n represent the temperature, area of Schottky contact, Richardson's constant, Schottky barrier height, electron charge, Boltzmann's constant, and ideality factor, respectively. From eqn (2), Φ_B can be expressed as:

$$\Phi_B = \frac{k_BT}{q}\ln\left(\frac{AA^*T^2}{I_S}\right) \quad (3)$$

Under a target gas ambient, the variations in Schottky barrier height can be expressed as:

$$\Delta\Phi_B = \Phi_{B(air)} - \Phi_{B(gas)} \quad (4)$$

where $\Phi_{B(air)}$ and $\Phi_{B(gas)}$ are the Schottky barrier heights in air and the environment of the target gas, respectively. Hence, the response sensitivity (S_R) of the GaN-based gas sensor can be calculated as:[43,44]

$$S_R = \frac{|I_{(air)} - I_{(gas)}|}{I_{(air)}} = \frac{|\Delta I|}{I_{(air)}} \quad (5)$$

where $I_{(air)}$ and $I_{(gas)}$ are the current of the Schottky diode in air and the ambience of the target gas, respectively. Therefore, the variation in current (ΔI) is dependent on the Schottky barrier height changes $\Delta\Phi_B$.

Due to the aforementioned characteristics, GaN-based Schottky diodes have enabled the detection of gases such as H_2, H_2S, NH_3, CH_4, acetone (C_3H_6O), and NO_2, as shown in Fig. 1. In 2008, Song *et al.* fabricated H_2 sensors with a Pt/AlGaN/GaN Schottky diode structure; the device could work in a wide range of temperatures (25–800 °C). The schematic of the device is depicted in Fig. 1(a).[32] The experimental examination of its performance in terms of detecting hydrogen at concentrations ranging from 0.5 ppm to 5000 ppm verified its decent sensing performance at high temperatures. This corroborates the suitability of GaN sensors for harsh environments. As the temperature increased, the response sensitivity S_R of the device improved owing to the more effective dissociation of H_2 on the surface of Pt, and this induced larger variations in the Schottky barrier height $\Delta\Phi_B$. At a fixed concentration of 5000 ppm, the S_R of the device improved from 0.3 at 25 °C and 0.8 at 300 °C to 2.1 at 600 °C, and then saturated to 2.2 at 700 °C and 800 °C. The device also exhibited a fast response time of 1.6 s and a recovery time of 10.3 s at 800 °C at a H_2 concentration of 5000 ppm. Xiao *et al.* proposed a Pt/GaN-based Schottky diode sensor for hydrogen sulfide (H_2S) in 2015.[45] The main structure on the substrate was a Schottky contact formed by Pt and GaN, which was separated from an Ohmic contact as shown in Fig. 1(b). The device could detect diluted H_2S with a concentration close to 0.05 ppm at 200 °C, and exhibited a fast response time of around 10 s when the concentration of H_2S was higher than 1 ppm. In 2020, Chang *et al.* demonstrated a Pt nanoparticles (NPs)/Pt film-based AlGaN/GaN Schottky diode sensor for ammonia (NH_3), as shown in Fig. 1(c).[46] The size of these Pt NPs ranged from approximately 330 nm to 380 nm (as shown in the inset SEM image in Fig. 1(c)). The Pt nanoparticles effectively increased the surface area-to-volume ratio of the device, and this gave rise to a spillover effect of hydrogen atoms that enhanced the catalytic reactivity of the Pt film. Owing to the synergistic catalytic activity of Pt NPs and the Pt thin film, the device could accurately detect ammonia. It exhibited a high sensing response of 522.1 under 1000 ppm NH_3/air at 473 K and an extremely low level of detection of 0.4 ppm NH_3/air. These metal nanoparticle-based Schottky diode devices are promising for applications that require a high sensing response and a low limit of detection because of their excellent performance and simple structure. A similar structure, shown in Fig. 1(d), was proposed by Xi *et al.* in 2013. They used a Pt anode in a GaN-based Schottky diode sensor to detect methane (CH_4).[47] Methane is a hazardous, odorless, and colorless gas with a lower explosive limit and an upper explosive limit

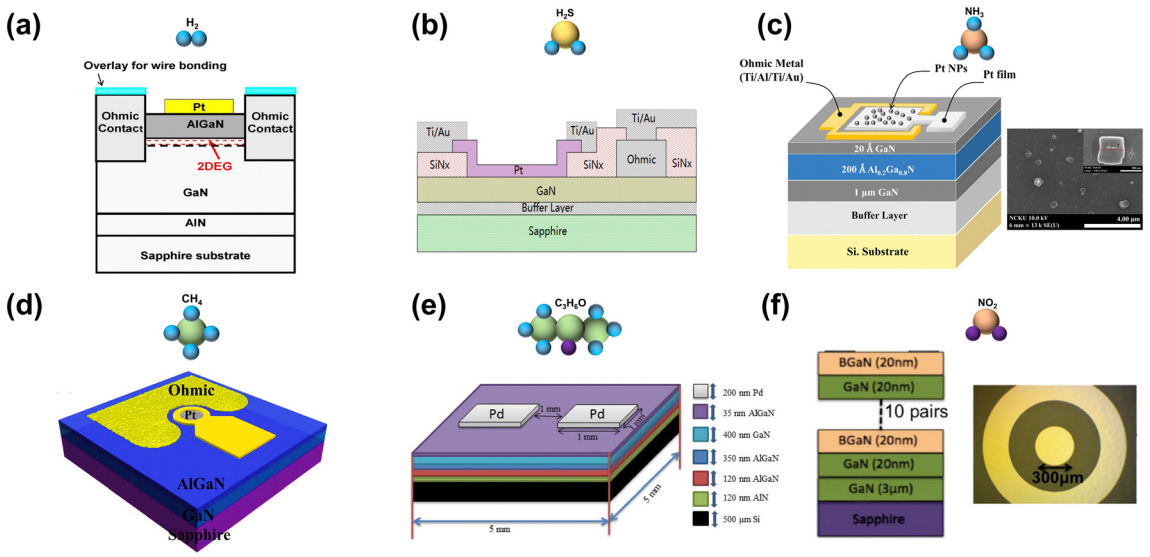

Fig. 1 GaN-based Schottky diode-type gas sensors. (a) Pt-based AlGaN/GaN/sapphire H_2 sensor (reproduced from ref. 32 with permission from IEEE. Copyright 2008, IEEE).[32] (b) Pt-based GaN/sapphire H_2S sensor (reproduced from ref. 45 with permission from IOP Publishing. Copyright 2015, IOP Publishing).[45] (c) Pt-nanoparticles (NPs)/Pd-film-based GaN/AlGaN/GaN/Si NH_3 sensor (reproduced from ref. 46 with permission from IEEE. Copyright 2020, IEEE).[46] (d) Pt-based AlGaN/GaN/sapphire CH_4 sensor (reproduced from ref. 47 with permission from the AIP Publishing. Copyright 2013, AIP Publishing).[47] (e) Pd-based AlGaN/GaN/Si acetone (C_3H_6O) sensor (reproduced from ref. 48 with permission from IEEE. Copyright 2017, IEEE).[48] (f) Pt-based BGaN/GaN superlattice/sapphire NO_2 sensor (reproduced from ref. 49 with permission from AIP Publishing. Copyright 2015, AIP Publishing).[49]

of 5.3% and 14.3%, respectively, at room temperature. When exposed to 10 000 ppm CH_4 at 400 °C (673 K), the device exhibited a sensitivity of 1 under the reverse-bias condition, much higher than that under the forward-bias condition. The response and recovery times of the sensor, defined as the diode current rising and falling to 90% of its saturation value, respectively, were on average 160 s and 220 s. These results verify its capability of detecting methane under both reverse and forward biases, as well as its strong potential for use in high-temperature applications. In 2017, Das *et al.* grew an AlGaN/GaN heterostructure using plasma-assisted molecular beam epitaxy (PAMBE). They utilized a Pd Schottky contact, enabling it to function as an acetone sensor (shown in Fig. 1(e)).[48] The device was characterized by field-emission scanning electron microscopy (FESEM) to obtain the surface morphology of AlGaN, which showed the single crystalline quality of both AlGaN and GaN. The sensing performance of the device was measured in the temperature range of 100 °C to 250 °C and a gas concentration range of 100 ppm to 1000 ppm. At an optimum temperature of 150 °C, the sensor showed response magnitudes of 62.41%, 80.58%, 86.42%, and 95.02% for 100, 400, 700, and 1000 ppm acetone, respectively. It also showed a fast response time of ~18–44 s, while its recovery time was ~25–109 s under different temperature and concentration conditions. The low cross-sensitivity of the device to other interfering species, such as butanone, benzene, toluene, and xylene, indicated its selectivity for acetone. More interestingly, in 2015, Bishop *et al.* found that BGaN/GaN superlattice-based double-Schottky junction sensors (Fig. 1(f)) for detecting NO_2 yielded better performance than the GaN-based Schottky diode.[49] The BGaN layer on the surface increased its trap density and depth, which in turn improved the responsivity and high-temperature stability of the device, while the GaN layer improved the magnitude of the diode current. The BaGN/GaN sensor recorded a response sensitivity of approximately 0.3, 10 times higher than that of the reference GaN sensor. Moreover, the response and recovery times of the BaGN/GaN sensor were 5 s and 80 s, respectively, shorter than those of the GaN sensor (response and recovery times of around 300 s). These results prove that the BaGN/GaN NO_2 sensor is a better choice for balancing sensitivity and responsivity. Table 1 provides a comprehensive summary of recent results obtained using GaN-based Schottky diode gas sensors.

2.2. HEMT structure sensors

Compared with Schottky diode sensors, sensors based on field-effect transistors (FETs) have several advantages, such as amplified signals, extensive range of linear detection, and the capacity for simple integration with peripheral electronic devices.[4] Moreover, HEMT-based sensors with the AlGaN/GaN heterostructure deliver good performance due to the transistor's properties and the presence of 2-DEG. First, the response current is higher than that in Schottky diodes owing to the high carrier density of 2-DEG, and this leads to a lower detection limitation.[76–79] Second, HEMTs provide the possibility of adjusting the gate voltage to control the drain current, which in turn allows for the gate bias to be used to optimize the sensitivity, making it more robust than diode-type sensors. Furthermore, the separation of the current-carrying 2-DEG from the sensing surface means that under operation, the current flowing through the 2-DEG does not interfere with the gas-sensing function.[79] Finally, AlGaN/GaN heterostructure-based sensors are suitable for integration with other electronic and optoelectronic devices to form more multi-modal edge smart integrated chips.[11,12,80] By modifying the gate area, HEMT devices can be designed to target and detect a wide range of gases, making them highly versatile and adaptable for various gas sensing applications. One limitation of AlGaN/GaN HEMT-based sensors is their inherent "normally on" characteristic which results in increased standby power consumption. This issue can be partly solved by lowering the bias voltage of the sensor.[13,81]

Similar to Si-based metal oxide semiconductor field effect transistors (MOSFETs), the GaN HEMT sensor serves as a three-terminal device. The drain current (I_{DS}) of an AlGaN/GaN-based HEMT can be expressed as:[82,83]

$$I_{DS} = \frac{\mu C_b W}{2L}\left[2(V_G - V_T)V_D - V_D{}^2\right] \quad (6)$$

where μ is the mobility of 2-DEG, W/L is the gate width/length, and C_b is the gate-to-channel capacitance, which is the sum of the contributions of each layer between the gate metal and 2-DEG to capacitance. For AlGaN/AlN/GaN heterostructures, $1/C_b = (1/C_{AlGaN} + 1/C_{AlN} + 1/C_{2\text{-}DEG})$. V_G, V_D, and V_T are the gate voltage, drain voltage, and threshold voltage of the device, respectively.

When $V_D \geq V_G - V_T$, the device operates in the saturation region, and the saturation drain current can then be given as:

$$I_{DS} = \frac{\mu C_b W}{2L}(V_G - V_T)^2 \quad (7)$$

We introduce the expression for the V_T of an AlGaN/GaN HEMT:

$$V_T = \Phi_B - \frac{\Delta E_C}{q} - \frac{q n_s}{C_b} \quad (8)$$

where Φ_B is the Schottky barrier height, ΔE_C is the discontinuity in the conduction band, q is the elementary charge, and n_s is the carrier density of the sheet charge. The Schottky barrier height is dependent on the work function (Φ_m) of the gate metal and the electron affinity of the semiconductor (χ_s), $\Phi_B = \Phi_m - \chi_s$. When HEMT-based sensors are exposed to the target gas, the variations in Schottky barrier height $\Delta\Phi_B$ induce variations in ΔV_T. Under a fixed V_G, alterations in the threshold voltage will result from shifting concentrations of gases present in the environment. Consequently, measuring changes in the drain current enables the determination of both the concentration levels and the identity of the detected components.

GaN-based HEMT devices have been used to detect H_2, H_2S, NH_3, CH_4, acetone (C_3H_6O), NO_2, CO, CO_2, and O_2, as shown in Fig. 2. In 2017, Sokolovskij *et al.* proposed a Pt gate HEMT-based H_2 sensor shown in Fig. 2(a).[84] The effective interaction area between the Pt gate metal and the H_2 molecule was

Table 1 Comparisons of sensing performance of the GaN-based Schottky diode gas sensors (T: optimal temperature, S_R: response sensitivity, τ_a: response time (time constant), τ_b: recovery time (time constant), NPs: nanoparticles, NNs: nanonetworks, NSs: nanostructures, NRs: nanorods, EP: electroless plating, and SL: superlattice)

Device structure	Gas type	Detection range (ppm)	T (K)	S_R	τ_a (s)	τ_b (s)	Ref.
Pt/GaN/sapphire	H_2	2.5–25 000	673	—	—	—	37
Pd NPs/Pd/AlGaN/GaN/sapphire	H_2	0.8–10 000	300	4.2×10^6	128	49	42
Pt/GaN/sapphire	H_2	70–10 000	583	—	9	15	50
Pd/AlGaN/GaN/sapphire	H_2	15.2–9660	423	2.04×10^5	7	6	51
Pd/GaN/sapphire	H_2	14–9970	300	1.27×10^4	14	9	41
Pd/GaN/sapphire	H_2	5–10 000	303	2.05×10^5	370	—	52
Pd/GaN/sapphire	H_2	14–9970	570	—	10.5	5	53
Pt/GaN/InGaN/Si	H_2	429–810	573	0.11	25.1	34.1	54
Pt NNs/AlGaN/GaN/sapphire	H_2	40 000	298	2.3×10^5	<5	—	55
Pt NNs/AlGaN/GaN/sapphire	H_2	0.1–40 000	298	5.79×10^5	4	251	56
Pd NSs/AlGaN/GaN/sapphire	H_2	0.01–10 000	300	1454	16.2	11.2	57
Pt NPs/Pt/AlGaN/GaN/Si	H_2	1–10 000	300	2.7×10^6	17	23	27
Pt/AlGaN/GaN/sapphire	H_2	50 000	1073	1.75	—	—	58
Pt/AlGaN/GaN/sapphire	H_2	50 000	1073	1.5	—	—	59
IrPt/AlGaN/GaN/sapphire	H_2	50 000	973	4	—	—	59
PdAg/AlGaN/GaN/sapphire	H_2	50 000	473	2	—	—	59
Pt/AlGaN/GaN/sapphire	H_2	500	298	2.8×10^3	<4	—	60
Pt/AlGaN/GaN/sapphire	H_2	500	298	964	—	—	61
Pt/AlGaN/GaN/sapphire	H_2	0.5–5000	1073	2.2	1.6	10.3	32
Pt/AlGaN/GaN/sapphire	H_2	1000–10 000	298	—	14	—	62
Pd/GaN/sapphire	H_2	5–10 000	303	2.12×10^5	178	26	63
Pd: SiO_2/GaN/sapphire	H_2	1080–10 100	300	7.7×10^6	35	—	64
Pt NPs: SiO_2/Pt/AlGaN/GaN/Si	H_2	0.1–10 000	298	7.3×10^5	27	—	65
Pd/AlGaN/GaN/sapphire	H_2	50–1000	473	9.09×10^4	3	20	66
Pt/GaN/sapphire	H_2S	0.05–1	473	—	10	—	45
Pt/GaN/sapphire	H_2S	0.1–10	473	—	3	—	67
EP Pt/AlGaN/GaN/sapphire	NH_3	0.01–1000	388	16.22	523.8	122.4	68
Pt/AlGaN/GaN/sapphire	NH_3	35–10 000	423	182.7	217.7	62.6	69
Pt NPs/Pt/GaN/AlGaN/GaN/Si	NH_3	0.4–1000	473	522.1	308	125	46
Pt/AlGaN/GaN/sapphire	NH_3	35–10 000	473	183	$\sim$100	31.3	70
ZnO NRs/AlGaN/GaN/sapphire	NH_3	0.1–2	573	0.1259	$\sim$10	$\sim$10	71
Pt/AlGaN/GaN/sapphire	NH_3	35–1000	473	90.81	134	27	66
Pt/AlGaN/GaN/sapphire	CH_4	5000–20 000	673	1	160	220	47
Ni/GaN/sapphire	CH_4	50 000–150 000	773	0.875	<3	—	72
GaN/sapphire	CH_4	10 000	473	0.2	10	60	73
Pd/AlGaN/GaN/Si	Acetone	100–1000	423	0.58	—	—	74
Pd/AlGaN/GaN/Si	Acetone	100–1000	523	8.84	22.81	80.28	33
Ni/InGaN/GaN/Si	Acetone	100–400	373	1.034	8.4	19.1	75
Pd/AlGaN/GaN/Si	Acetone	100–1000	523	0.95	44	46	48
Pt/GaN/sapphire	NO_2	90–450	473	0.032	300	300	49
Pt/BGaN/GaN SL/sapphire	NO_2	90–450	523	0.3	5	80	49

defined by the length L and width W of the gate. They proposed optimizing the device layout to enhance the capacity for hydrogen sensing. The design process involved adjusting the ratio of the gate's width to its length (W/L) between 0.25 and 10. After fabrication, the device was tested at 200 °C in a hydrogen ambient. The results showed a 217% increase in its sensitivity and a 4630% increase in response current variations at 500 ppm H_2 when W/L was increased from 0.25 to 10. This showed that a higher W/L ratio resulted in a higher response sensitivity and current variations that were consistent with the expression for the drain current (eqn (6)). Because the current variations were more significant at a higher W/L ratio, a lower detection limit of 5 ppm was obtained at W/L = 10. However, the transient characteristics detailed in this study involved a trade-off between the response/recovery times and the W/L ratio. For example, a higher W/L ratio led to a faster response time but a slower signal recovery time with respect to the baseline value. After layout optimization, Sokolovskij *et al.* proposed an H_2S sensor in 2018 with the structure shown in Fig. 2(b). The optical micrograph shows the top view of the fabricated sensor with a W/L ratio of 10.[83] The H_2S sensor could operate at a high temperature (150–250 °C) over a wide range of biasing conditions (V_G from −3 V to 1 V). It achieved a high response sensitivity of 1.12 for 90 ppm of H_2S and the lowest detection limit of 15 ppm at 200 °C, showing its capability to detect low concentration of H_2S to ensure the safety of energy industries. Watanabe *et al.* used Pd as the sensing material to develop a Pd/AlGaN/GaN HEMT-type sensor that could detect various concentrations of hydrogen (H_2), methane (CH_4), and propane (C_3H_8) (Fig. 2(d)).[85] They found that each gas had a characteristic spectrum of sensitivity to temperature at different peak positions owing to their different decomposition temperatures. When the gas concentration was 1000 ppm, the highest response sensitivities of H_2, CH_4, and C_3H_8 were all around 0.78, but the optimized temperatures at their maximum sensitivity were 230 °C, 350 °C, and 310 °C, respectively. Pt and Pd are commonly used gate materials for GaN HEMT-based gas sensors. Moreover, metal–oxide gates, such as ZnO, WO_3, TiO_2,

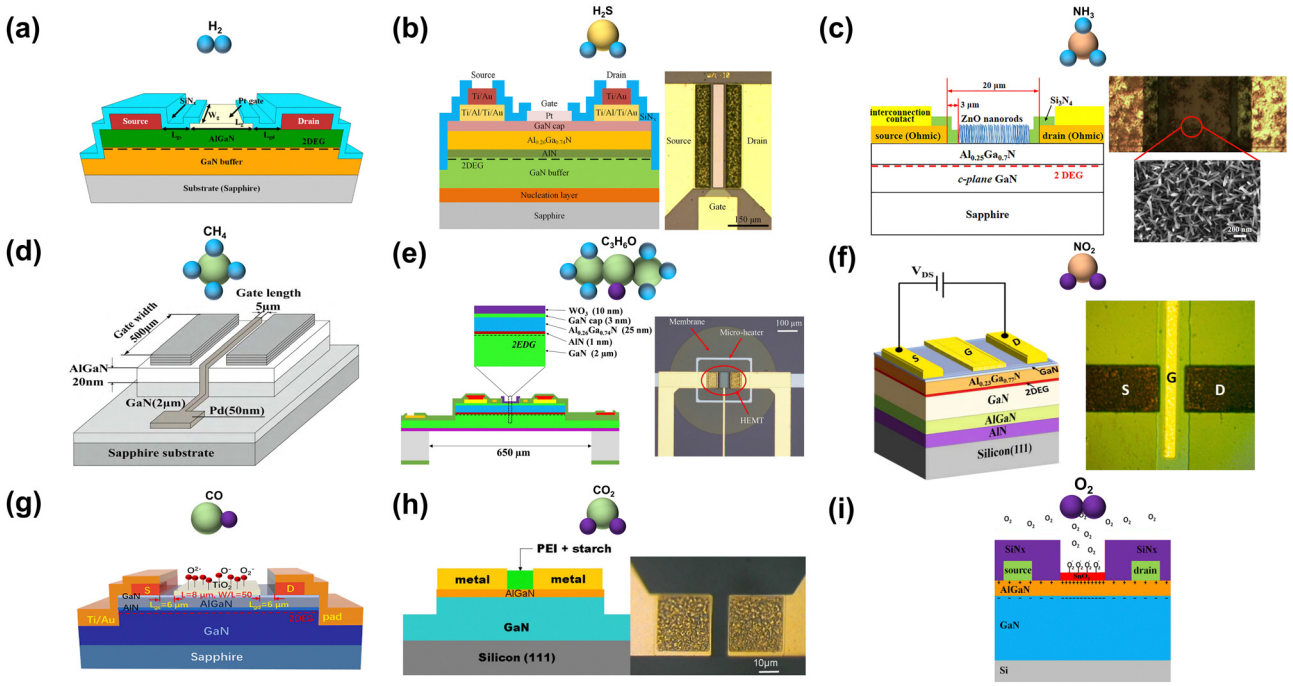

Fig. 2 GaN-based HEMT-type sensors. (a) Pt-based AlGaN/GaN/sapphire H_2 sensor (reproduced from ref. 84 with permission from IEEE. Copyright 2017, IEEE).[84] (b) Pt-based AlGaN/GaN/sapphire H_2S sensor (reproduced from ref. 83 with permission from Elsevier. Copyright 2018, Elsevier).[83] (c) ZnO nanorod-based AlGaN/GaN/sapphire NH_3 sensor (reproduced from ref. 86 with permission from AIP Publishing. Copyright 2017, AIP Publishing).[86] (d) Pd-based AlGaN/GaN/sapphire CH_4 sensor (reproduced from ref. 84 with permission from IEEE. Copyright 2012, IEEE).[85] (e) WO_3-based AlGaN/GaN/Si acetone (C_3H_6O) sensor (reproduced from ref. 76 with permission from IEEE. Copyright 2019, IEEE).[76] (f) MoS_2-based AlGaN/GaN/Si NO_2 sensor (reproduced from ref. 89 with permission from Elsevier. Copyright 2022, Elsevier).[89] (g) TiO_2-based AlGaN/GaN/sapphire CO sensor (reproduced from ref. 28 with permission from Elsevier. Copyright 2022, Elsevier).[28] (h) PEI/Starch-based AlGaN/GaN/Si CO_2 sensor (reproduced from ref. 90 with permission from AIP Publishing. Copyright 2012, AIP Publishing).[90] (i) SnO_2-based AlGaN/GaN/Si O_2 sensor (reproduced from ref. 87 with permission from AIP Publishing. Copyright 2012, AIP Publishing).[87]

and SnO_2, are widely used for gas sensing, as shown in Fig. 2(c), (e), (g) and (i). Jung *et al.* fabricated a functionalized ZnO nanorod gate-based NH_3 sensor, shown in Fig. 2(c), in which the ZnO nanorods were grown through a hydrothermal method and etched off around the gate and the area of the contact pad.[86] The device exhibited complete selectivity for 2 ppm of NH_3 over 100% O_2, 10% CO_2, 0.1% CO, 4% CH_4, and 0.05% NO_2 under the same conditions of detection at 25 °C. The device showed the lowest detection limit of 0.1 ppm and a working temperature of up to 300 °C, and its response time was shorter than 1 s and recovery time was around 40 s at 300 °C. This verified its good sensing performance. In 2012, Hung *et al.* grew SnO_2 by using a hydrothermal selective-area deposition method in the gate region to detect O_2, as depicted in Fig. 2(i).[87] The SnO_2 nanomaterials were annealed at 400 °C for 2 h in air to increase their grain size, which in turn enhanced their sensitivity to the gas owing to a higher specific conductivity of the grain boundary. The device exhibited a wide O_2 concentration detection range, from 1.04% to 20.8% at 100 °C, with milliampere order drain current variations. This offers a promising way to construct O_2 sensors with a low detection limit, a low operating temperature, and low power consumption. The oxide gate material can also be deposited using e-beam evaporation or sputtering technology. Fan *et al.* fabricated a CO sensor by using an e-beam-evaporated TiO_2 gate as shown in Fig. 2(g).[28] The chemisorption of the oxygen species O^-, O_2^-, and O^{2-} on the surface of TiO_2 led to a reaction with CO molecules to form CO_2 and the release of electrons back into the TiO_2 film, resulting in drain current variations. They found that O_2 plasma-treated TiO_2 enhanced oxidation by the oxygen species to improve the response sensitivity of the sensor without damaging the surface morphology and increasing roughness. Compared with the untreated sample, the plasma-treated sample had an extremely low detection limit of CO down to 10 ppb. The detection range of the CO sensor at 270 °C was 0.01 ppm (10 ppb)–500 ppm, with a response time of 4 s and a recovery time of 80 s at a CO concentration of 100 ppm. The selectivity and endurance of the device reflected good selectivity between CO and CO_2, and no prominent degradation in its performance was noted after 10 days. Additional power consumption is needed to satisfy the requirement of detection of the sensor at high temperatures. To reduce power consumption, Offermans *et al.* proposed a suspended ultra-low-power AlGaN/GaN membrane device for monitoring air quality in which the Si substrate was etched away between the bonding pads. This led to a suspended membrane with an area of 1.6 × 1.8 mm^2 to reduce power consumption.[88] Moreover, Sun *et al.* integrated a WO_3-gated AlGaN/GaN HEMT acetone sensor with a microheater, as shown in Fig. 2(e).[76] The silicon substrate was etched away under a microheater, and this led to the formation

of a membrane and a suspended structure of the sensor. This significantly reduced thermal loses due to heat conduction through the substrate. The temperature could be adjusted by controlling the voltage bias of the microheater, and could be increased to 300 °C. The sensor had a power consumption of only 200 mW. Due to the presence of the microheater, the response sensitivity of the sensor to acetone was 25.7%, and the variation in the drain current was 0.31 mA under 1000 ppm acetone at 300 °C, with a response time of 48 s and a recovery time of 320 s. The excellent repeatability of its sensing response, and its acceptable selectivity among ethanol, ammonia, and CO were verified. Other promising gas-sensitive materials have also been explored. Sharma *et al.* synthesized an MoS_2 gate on AlGaN/GaN HEMTs through the hydrothermal method to develop an NO_2 gas sensor (Fig. 2(f)).[89] The MoS_2 layer could overcome obstacles in monitoring toxic gases present in the atmosphere at room-temperature, and it enhanced the response sensitivity and selectivity of the sensor. The proposed device operated at 25 °C with a detection range of NO_2 from 1 ppm to 100 ppm. Its response sensitivity reached 0.405, with a response time of 118 s and a recovery time of 142 s at an NO_2 concentration of 1 ppm. A high NO_2 selectivity was achieved compared to other gases species (H_2S, CO_2, and H_2). These findings show that the sensor using MoS_2 on the HEMT platform can quickly detect NO_2 with a high response and selectivity at room temperature without consuming thermal energy. An AlGaN/GaN HEMT functionalized with polyethylenimine (PEI)/starch for the detection of CO_2, with a wide dynamic range of 0.9–50%, was studied by Chang *et al.* as shown in Fig. 2(h).[90] Starch was added to the PEI to enhance the absorption of water molecules by the PEI/starch thin film. The primary amine groups, $-NH_2$, on the main chain of PEI reacted with CO_2 as well as the water-forming $-NH_3^+$ ions and $OCOOH^-$ ions, and this induced charge variation in the PEI layer and in turn changed the drain current. The response times were ~100 s for all concentrations of CO_2 at 108 °C. This verified a suitable paradigm for detecting CO_2 by using a compact GaN-based HEMT chip. Table 2 offers a side-by-side analysis of the gas sensing capabilities of AlGaN/GaN HEMT devices. Detailed information regarding various parameters is presented for ease of comparison.

2.3. MOS structure sensors

Compared to metal–gate structures, MOS diode and MOS HEMT gas sensors offer enhanced thermal stability. As such, they are suitable for utilization in conjunction with GaN materials to improve gas sensing performance.[14,39,130] To suppress surface leakage and enhance the stability of the device, numerous dielectrics—for example, NiO,[131] GaO_x ($AlGaO_x$),[132,133] SiO_2,[134] IrO_2,[135] HfO_2,[136] ZnO,[137] Ta_2O_5,[138] and Sc_2O_3[39]—have been proposed to develop MOS-type sensors. Moreover, the results of experiments have shown that the trapping of hydrogen atoms is accompanied by oxygen atoms on the surface of the semiconductor.[64,139] The introduction of an adsorptive oxide between the sensing material and the semiconductor improves the sensing response of the device; however controlling the thickness of the oxide gives rise to processing instability.[64]

Fig. 3 shows three typical MOS structure devices used as H_2, NH_3, and NO_2 sensors. Ahn *et al.* proposed a Pt-decorated graphene/SiO_2 gate AlGaN/GaN HEMT for highly sensitive H_2 detection (Fig. 3(a)).[140] Owing to its inherently large surface-to-volume ratio, subtle changes in charges invoked by noble metals contributed to variations in the conductivity of graphene, thereby resulting in good hydrogen selectivity. The randomly located island-like Pt at the top of the gate acted as a catalyst for hydrogen. The conductive graphene layer maintained an equipotential across the entire region of the gate, and the SiO_2 gate insulator reduced leakage and increased surface absorption. When hydrogen gas was introduced, the Pt catalyst broke the hydrogen molecules into hydrogen ions, and their subsequent diffusion to the graphene/SiO_2 interface led to the formation of a dipole layer that affected the density of 2-DEG. The device exhibited ultra-high response sensitivities of approximately 1.6×10^7 at 1000 ppm H_2 and 15.4 at 1 ppm H_2 under an optimum gate bias. This can be attributed to the thin island-like Pt layer that enabled efficient dissociation of hydrogen molecules and diffusion of hydrogen atoms to the gate, as well as the larger number of absorption sites offered by the graphene/SiO_2 interface. In a selectivity test where the device was exposed to 100 ppm H_2, NH_3, H_2S, and CO, the variation in the drain current after exposure to H_2 was almost 1000 times higher than that when it was exposed to NH_3 and H_2S. The drain current did not vary significantly when the device was exposed to CO, which further proves that the Pt-decorated graphene layer yielded good selectivity for hydrogen. Electroless plating (PE) and treatment with H_2O_2 were carried out by Liu *et al.* to develop a Pt/GaO_x/AlGaN/GaN MOS Schottky diode NH_3 sensor, as shown in Fig. 3(b).[141] Compared with conventional thermal evaporation (TE) that can easily lead to thermal damage to the surface and degrade the performance of the sensor, EP is a low-temperature and energy-efficient technology to improve the metal–semiconductor interface and enhance the gas sensing performance. Combined with the GaO_x layer oxidized by H_2O_2, it was able to suppress the leakage current and provide a large number of sites for gas absorption. When it was exposed to NH_3, the gas molecules were adsorbed on the Pt metal, and some of them were dissociated into H_2 and N_2. The H_2 molecules were further dissociated into H atoms, and some of them diffused through the bulk Pt to eventually accumulate at the Pt/GaO_x interface. This led to changes in the drain current. The response sensitivity of the device was 22.3 in 1000 ppm NH_3 at 300 K, and rose to 678.4 when the temperature was increased to 423 K. Its response time and recovery time also decreased from 251 s to 183 s, and from 108 s to 34 s, respectively, under the same gas concentration. The sensitivity to 200 ppm NH_3, 10 000 ppm CH_4, 1000 ppm C_2H_5OH, and 100 ppm NO_2 at 423 K was 202, 0.73, 1.88, and 0.1, respectively, indicating excellent NH_3 selectivity. Hsu *et al.* proposed an ZnO-based Schottky diode sensor for NO_2, as shown in Fig. 3(c), in which the ZnO layer under the Au electrode reduced the leakage current.[66] The sensitivity of the sensor was 21.51 for 100 ppm NO_2 at 200 °C. However, its sensitivity was negatively correlated with temperature, and decreased to 4.36 when the temperature was increased to 300 °C. The transient response

Table 2 Comparisons of the sensing performance of AlGaN/GaN HEMT-based gas sensors (T: temperature, S_R: response sensitivity, τ_a: response time (time constant), τ_b: recovery time (time constant), NWs: nanowires, NSs: nanostructures, NNs: nanonetworks, NRs: nanorods, and EP: electroless plating)

Device structure	Gas type	Detection range (ppm)	T (K)	S_R	τ_a (s)	τ_b (s)	Ref.
Pt/AlGaN/GaN/sapphire	H_2	0–5000	573	—	—	—	38
Pt/AlGaN/GaN/Si	H_2	0.06–10 000	423	221.01	2.5	—	91
Pt/AlGaN/GaN/sapphire	H_2	100 000	300	0.2	—	—	92
EP-Pd/AlGaN/GaN/sapphire	H_2	200–10 000	600	—	—	—	93
Pd/AlGaN/GaN/Si	H_2	0.05–20 000	393	191.37	2–3	—	94
Pt/AlGaN/GaN/sapphire	H_2	100–5000	473	0.1	—	—	95
Pd/AlGaN/GaN/sapphire	H_2	1–10 000	303	—	9	15	96
Pt/AlGaN/GaN/sapphire	H_2	2–6216	403	1.18	—	—	97
EP-Pt/AlGaN/GaN/sapphire	H_2	5–10 000	400	0.137	28	36	98
Pt NNs/AlGaN/GaN/sapphire	H_2	500	298	3.3×10^4	<5	—	99
Pt/AlGaN/GaN/Si	H_2	40 000	623	0.33	—	—	100
Pd/AlGaN/GaN/sapphire	H_2	50–10 000	303	—	9	15	101
Pt/AlGaN/GaN/sapphire	H_2	0.5–5000	873	6251	—	—	102
Pd/AlGaN/GaN/Si	H_2	1000–40 000	473	0.7268	3	—	81
Pd/AlGaN/GaN/sapphire	H_2	0.01–2000	303	0.158	13.8	20	103
EP-Pd/AlGaN/GaN/sapphire	H_2	5–10 000	300	—	—	—	104
Pd/AlGaN/GaN/sapphire	H_2	1–100	433	—	23	33	105
Pt/AlGaN/GaN/sapphire	H_2	5–500	473	0.076	342	1539	84
Pt/AlGaN/GaN/sapphire	H_2	5–300	513	0.422	258	816	106
SnO_2/AlGaN/GaN/sapphire	H_2	10 000	573	0.12	240	570	107
Pt/AlGaN/GaN/sapphire	H_2	0.01–5000	1073	4658	—	—	108
Pd/AlGaN/GaN/Si	H_2	1000–40 000	473	0.8	<0.4	12.4	109
Pt/AlGaN/GaN/sapphire	H_2	5–300	513	1.457	150	531	110
Pd/AlGaN/GaN/sapphire	H_2	10–1000	623	0.78	—	—	85
AlGaN/GaN/Si	H_2	300–3000	423	0.6	—	—	88
Pt/AlGaN/GaN/sapphire	H_2	15 000–100 000	773	0.65	19	137	111
Pt/AlGaN/GaN/sapphire	H_2S	15–90	523	0.135	—	—	82
Pt/AlGaN/GaN/sapphire	H_2S	15–90	473	1.12	219	507	83
Pt/AlGaN/GaN/sapphire	H_2S	15–90	523	—	—	—	112
Pt/AlGaN/GaN/sapphire	H_2S	0.5–80	523	0.08	56	2316	113
ZnO NDs/AlGaN/GaN/sapphire	NH_3	0.1–2	573	0.13	1	40	86
Pt/AlGaN/GaN/sapphire	NH_3	35–10 000	303	113.4	—	—	65
Pt/GaN/AlGaN/GaN/Si	NH_3	10–50	548	0.0083	<180	<360	114
Pt/AlGaN/GaN/sapphire	NH_3	0.15–15	573	0.007	—	—	79
Pt/AlGaN/GaN/sapphire	NH_3	1.5–15	873	0.33	27	—	115
AlGaN/GaN/Si	NH_3	1–12	548	0.08	—	—	88
Pd/AlGaN/GaN	CH_4	1000	623	0.6	—	—	85
WO_3/AlGaN/GaN/Si	Acetone	100–1000	573	0.257	48	320	76
Pt/AlGaN/GaN/sapphire	Acetone	30–120	573	0.027	30	—	116
Pt/AlGaN/GaN/sapphire	NO	10–810	673	0.07	—	—	79
Pt/AlGaN/GaN/sapphire	NO	100–900	873	0.24	25.8	—	115
Au/Ti/AlGaN/GaN/sapphire	NO_2	0.5–15	423	—	—	—	112
MoS_2/AlGaN/GaN/Si	NO_2	1–100	298	0.567	118	142	89
Pt/AlGaN/GaN/Si	NO_2	1–200	573	0.035	75	200	77
AlGaN/GaN/Si	NO_2	0.007–0.09	294	250	—	—	117
AlGaN/GaN/Si	NO_2	0.06–0.5	—	—	—	—	118
Pt/AlGaN/GaN/sapphire	NO_2	10–800	673	0.17	—	—	79
Pd/AlGaN/GaN/Si	NO_2	1–100	773	0.081	6	7	119
SnO_2/AlGaN/GaN/Si	NO_2	0.05–0.5	523	0.13	165	280	120
Pd/AlGaN/GaN/Si	NO_2	10–100	573	0.454	9	48	121
Pt/AlGaN/GaN/Si	NO_2	0.5–10	573	0.055	<120	<300	122
Pt/AlGaN/GaN/Si	NO_2	0.05–10	548	0.051	56	285	29
AlGaN/GaN/Si	NO_2	0.007–0.1	294	—	1800	18 000	123
Pt/AlGaN/GaN/sapphire	NO_2	100	303	0.126	61	—	124
Pt/AlGaN/GaN/sapphire	NO_2	100–900	873	0.385	72	—	115
WO_3/AlGaN/GaN/Si	NO_2	0.1–100	573	0.011	88	132	78
AlGaN/GaN/Si	NO_2	0.01–0.1	523	1.5	60	—	88
TiO_2/GaN nanowire/Si	NO_2	0.001–500	293	0.133	140	160	125
AlGaN/GaN/Si	CO_2	1000–6000	298	—	—	—	88
PEI/Starch/AlGaN/GaN/Si	CO_2	9000–500 000	381	—	$\sim$100	—	90
ZnO NDs/AlGaN/GaN/sapphire	CO_2	300–100 000	573	0.0431	—	—	126
Pt/AlGaN/GaN/sapphire	CO	0–10 000	573	—	—	—	38
ZnO NDs/AlGaN/GaN/sapphire	CO	100–250	423	0.075	<100	<100	127
ZnO NDs/AlGaN/GaN/sapphire	CO	30–250	423	0.075	<100	<40	128
NSs AlGaN/GaN/Si	CO	100	373	0.33	94	44	129
ZnO NDs/AlGaN/GaN/sapphire	CO	50–500	398	0.0034	40	15	6
TiO_2/GaN/AlGaN/GaN/sapphire	CO	0.01–500	543	0.0154	4	60	28
Pt/AlGaN/GaN/sapphire	O_2	15 000–1 000 000	623	0.021	—	—	111
SnO_2/AlGaN/GaN/Si	O_2	10 400–208 000	373	$\sim$0.09	—	—	87

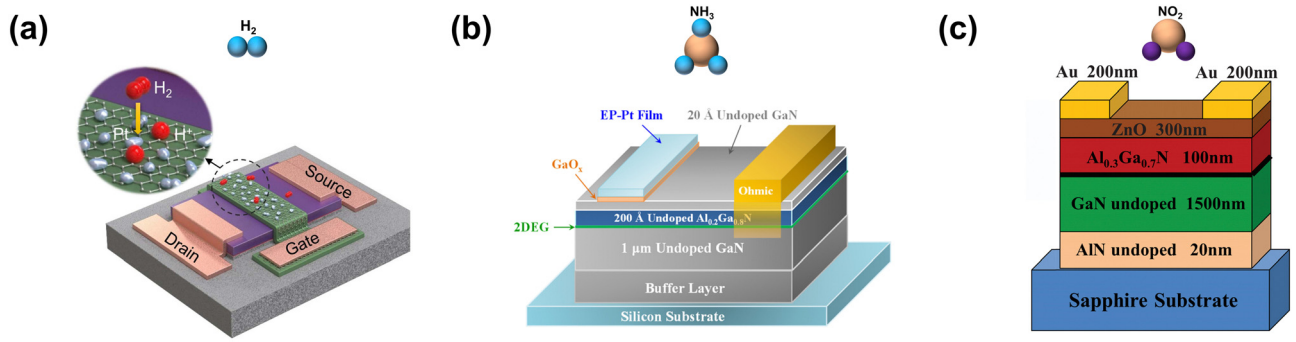

Fig. 3 GaN-based MOS-type sensors. (a) Pt/graphene/SiO_2-based AlGaN/GaN/sapphire MOS-HEMT H_2 sensor (reproduced from ref. 140 with permission from IEEE. Copyright 2021, IEEE).[140] (b) Pt/GaO_x-based AlGaN/GaN/Si MOS Schottky diode NH_3 sensor (reproduced from ref. 141 with permission from the American Chemical Society. Copyright 2019, American Chemical Society).[141] (c) ZnO-based AlGaN/GaN/sapphire MOS Schottky diode NO_2 sensor (reproduced from ref. 66 with permission from IOP Publishing. Copyright 2013, IOP Publishing).[66]

Table 3 Comparison of the sensing performance of MOS type gas sensors (T: temperature, S_R: response sensitivity, τ_a: response time (time constant), τ_b: recovery time (time constant), NPs: nanoparticles, and EP: electroless plating)

Device structure	Gas type	Detection range (ppm)	T (K)	S_R	τ_a (s)	τ_b (s)	Ref.
Pd/GaO_x/AlGaN/GaN/sapphire	H_2	0.1–10 000	300	1.8×10^5	13.3	23.6	132
Pd/$AlGaO_x$/AlGaN/GaN/sapphire	H_2	1–10 000	300	3.85×10^5	33	17	133
Pt/Sc_2O_3/AlGaN/GaN/sapphire	H_2	100 000	298	—	<1	—	39
Pd/NiO/AlGaN/GaN/Si	H_2	1–10 000	573	1.8×10^4	8	3	131
Pd/HfO_2/GaO_x/AlGaN/GaN/Si	H_2	5–10 000	300	8.47×10^5	36	35	142
Pt/GaO_x/AlGaN/GaN/Si	H_2	1–10 000	300	1.03×10^5	15	19	143
Pt/SiO_2/GaN/sapphire	H_2	4.3–9970	300	4.5×10^4	12	6	134
Pd/SiO_2/AlGaN/GaN/sapphire	H_2	5–10 000	343	3.3×10^5	7	—	144
Pd/HfO_2/AlGaN/GaN/Si	H_2	5–10 000	300	4.9×10^5	39	42	136
EP-Pd/GaO_x/AlGaN/GaN/sapphire	H_2	5–10 000	300	5.5×10^6	22	21	145
Pd NPs/Pt/GaO_x/AlGaN/GaN/Si	H_2	1–10 000	300	2.35×10^7	18	12	146
Pd NPs/Pd/GaO_x/AlGaN/GaN/Si	H_2	1–10 000	300	1.24×10^7	82	70.9	147
Pt NPs/Pd/GaO_x/AlGaN/GaN/Si	H_2	0.1–10 000	300	1.1×10^7	63	31	148
Pt/Sc_2O_3/AlGaN/GaN/sapphire	H_2	10 000–100 000	298	—	1	20	40
Pt/IrO_2/AlGaN/GaN/SiC	H_2	1000	373	—	205	179	135
Pt/Sc_2O_3/AlGaN/GaN/sapphire	H_2	100 000	298	—	<1	—	149
Pt/graphene/SiO_2/AlGaN/GaN/sapphire	H_2	1–1000	298	1.6×10^7	588	24	140
EP-Pt/GaO_x/AlGaN/GaN/Si	NH_3	0.4–1000	423	678.4	183	34	141
Pt/GaO_x/AlGaN/GaN/Si	NH_3	0.4–1000	473	252	288	120	30
Pt NPs/Pt/Ta_2O_5/AlGaN/GaN/Si	NH_3	0.1–1000	298	74.4	495	>5400	138
Pt/NiO/AlGaN/GaN/Si	NH_3	2–1000	423	244.2	2490	756	150
Pd/ZnO/GaN/sapphire	NO_2	10–100	523	—	60	120	137
Au/ZnO/AlGaN/GaN/sapphire	NO_2	20–100	473	21.51	288	525.6	66

and recovery times were 288 s and 525.6 s, respectively. Although these results do not allow for a direct comparison of performance between the metal–semiconductor structure (Schottky diode and HEMT) and the metal–oxide–semiconductor structure (MOS), the function of the inter-oxide layer is already fully known. These studies provide a novel opportunity for enhancing the sensitivity and selectivity of the sensor. A comparison of the sensing performance of MOS-based gas sensors is shown in Table 3.

3. Techniques of device fabrication

Fig. 4(a) and (b) show examples of the schematic fabrication of GaN-based Schottky and HEMT sensors. Because the GaN epitaxy technology on a bulk GaN substrate is an immature and expensive technology, the epitaxial structure is mostly grown on a Si or a sapphire substrate using a metal–organic chemical vapor deposition (MOCVD) system. The epitaxial structure typically consists of a several micron thick buffer layer to compensate for the stress induced by lattice mismatch, a GaN channel layer, and an AlGaN barrier layer to form the heterojunction and the 2-DEG channel. After epitaxial growth, the device fabrication begins with mesa isolation to separate individual sensors and avoid the signal crosstalk using an inductively coupled plasma reactive ion etching (ICP-RIE) system. The device samples are then rinsed with acetone, isopropanol, and deionized water to remove any particles and organic contaminants. The samples are dipped into an acid solution (hydrochloric acid or buffered oxide etch) to remove the native oxide from the AlGaN surface. An Ohmic-contact metal is then deposited on the patterned area of the AlGaN layer through

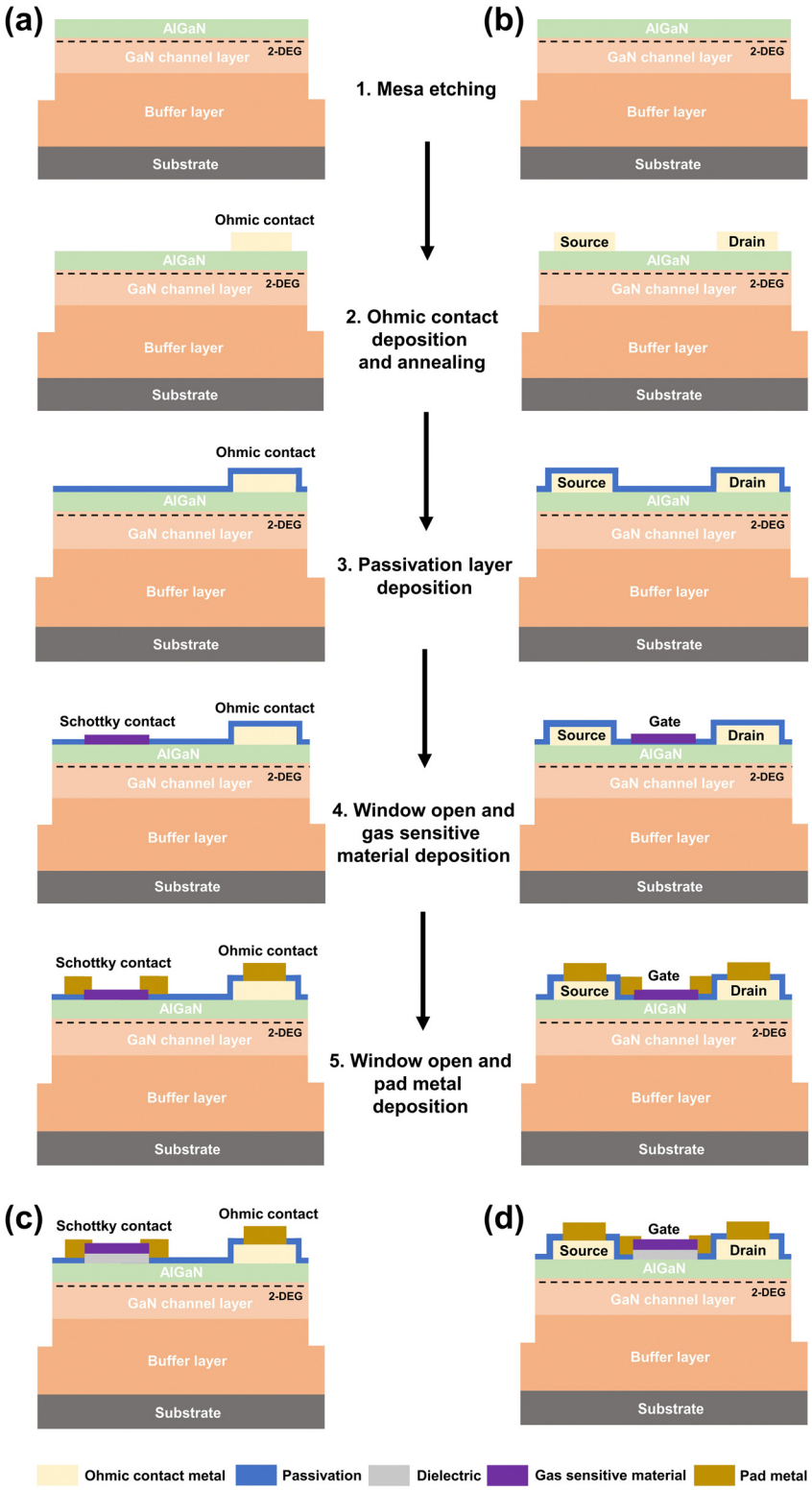

Fig. 4 Schematics showing the cross-sections of GaN-based gas sensors. The process of device fabrication: (a) Schottky diode-based sensors; (b) HEMT-based sensors. The cross-sectional schematics of MOS-type sensors: (c) MOS Schottky diode structure; and (d) MOS HEMT structure.

evaporation or sputtering. This is followed by annealing in an inert ambient environment, such as a rapid thermal annealing (RTA) system, to establish good ohmic contact. The passivation layer is deposited using a plasma-enhanced chemical vapor deposition (PECVD) system to reduce potential contamination and damage. The gas-sensitive material is deposited as the

Schottky contact for Schottky diode-type devices, and as the gate electrode for HEMT-type devices. For the MOS-type devices, a dielectric layer is first formed and the gas-sensitive material is then deposited above it, as shown in Fig. 4(c) and (d). Finally, a pad metal is deposited for wire bonding, packaging, and further testing.

4. Dynamic responses

In addition to the *I–V* characteristics of GaN-based gas sensors, their transient response-related characteristics also play an important role in determining their overall performance. These characteristics reveal the dynamic response of the gas sensor when target gas is injected and withdrawn. A typical output of a transient response curve is shown in Fig. 5, where I_0 is the baseline current of the sensor without the target gas, I_{max} is the saturation current at a specific gas concentration, I_t is the detection current at any time t during the gas-sensing period, and $t_{response}$ and $t_{recovery}$ are the intervals between the rise in current from I_0 to I_{max} and its decline from I_{max} to I_0, respectively. The definition of the response time ($t_{response}$) and the recovery time ($t_{recovery}$) is different in the literature, for example, the response time has been defined as the interval of increase from I_0 to 63%/70%/90% of I_{max}, while the recovery time has been defined as the interval of reduction from I_{max} to 37%/30%/10% of I_{max}.[63,64,83] The ideal gas sensor should have fast response and recovery times, and a large variation in the current (I_{max}–I_0). In this section, we begin with the discussion of dipole-induced sensing mechanism and the derivations of thermodynamical and kinetic equations. The factors influencing the response and recovery times, such as the temperature and gas concentration, are also mentioned to provide a better understanding to improve the dynamic performance of GaN-based gas sensors.

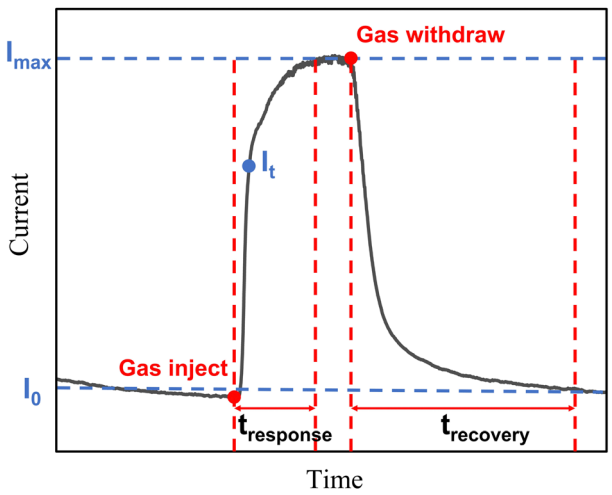

Fig. 5 Schematic illustration of the typical transient response test of the GaN-based gas sensor. The time-dependent currents reveal the dynamic response of the device when the target gas is injected and withdrawn. I_0 is the baseline current of the sensor without the sensing gas, I_{max} is the saturation current at a specific gas concentration, I_t is the detection current at any time t during the gas-sensing period, and $t_{response}$ and $t_{recovery}$ are the intervals of the rise in current from I_0 to I_{max}, and of its decline from I_{max} to I_0, respectively.

4.1. Dipole-induced sensing mechanism

As explained in Section 2, investigations have revealed that the Schottky barrier height modulation through various means leads to fluctuations in device current among all types of GaN-based gas sensors. This phenomenon serves as the foundation for their functionality. The inherent cause originates from the dipole-induced sensing mechanism. In GaN-based gas sensors, three primary gate configurations are commonly used. The first type leverages solely the properties of the AlGaN/GaN heterostructure for gas sensing purposes without any gas sensitive material.[73,88,117,118] This arrangement features an uncoated, exposed gate section, leading to direct modification of the 2-DEG density upon exposure to target gases. The second type employs metallic or oxidative materials on the gate, allowing for selective or multi-gas recognition while boosting the sensor performance. The third type of configuration using an oxidization layer interposed between the gate and the semiconductor (in MOS format) raises the number of adsorption sites at the metal/semiconductor interface, thereby enhancing gas sensitivity. However, all these configurations incorporating an oxide layer between the metal and semiconductor interfaces heighten the sensor's gas sensitivity. The last two configurations inevitably incorporate an oxide layer between the metal and semiconductor interfaces, since GaN-based materials undergo natural oxidation during fabrication, which heightens the sensor's gas sensitivity.[139,151]

Fig. 6 shows an HEMT-based gas sensor as an example. When the target gas is released, the gas molecules are chemisorbed on the gate surface, where interactions vary based on the chosen material. H_2 may be catalytically dissociated into H atoms by the Pt or the Pd gate. These H atoms are adsorbed on the surface as well as at any "internal" adsorption site, like the metal–semiconductor interface. Other gases, such as CO, can react with the O^2 species (O^{2-}, O_2^-, and O^-) on the surface of the TiO_2 gate.[28,106] These processes lead to alterations in the gate potential due to surface and interface dipoles, which in turn further influences the Schottky barrier height between the gate material and the AlGaN barrier layer resulting in current variations. The surface and interface dipole-induced potential changes can be represented using the Helmholtz model:[41,76,78,152]

$$\Delta V_{dipoles} = \frac{Np(\cos\theta)}{\varepsilon\varepsilon_0} \quad (9)$$

where N is the dipole density per unit area, p is the dipole moment, θ is the angle between the dipoles and the normal surface, ε is the relative permittivity of the gas molecules, and ε_0 is the permittivity of free space. The surface potential is primarily influenced by the value of p/ε of the polar molecules. Numerical calculation of the potential variation by solving for the dipole moments of the gas molecules is challenging. It is easier to directly determine changes in the Schottky barrier height change $\Delta\Phi_B$ by using eqn (3) and (4) for Schottky diode

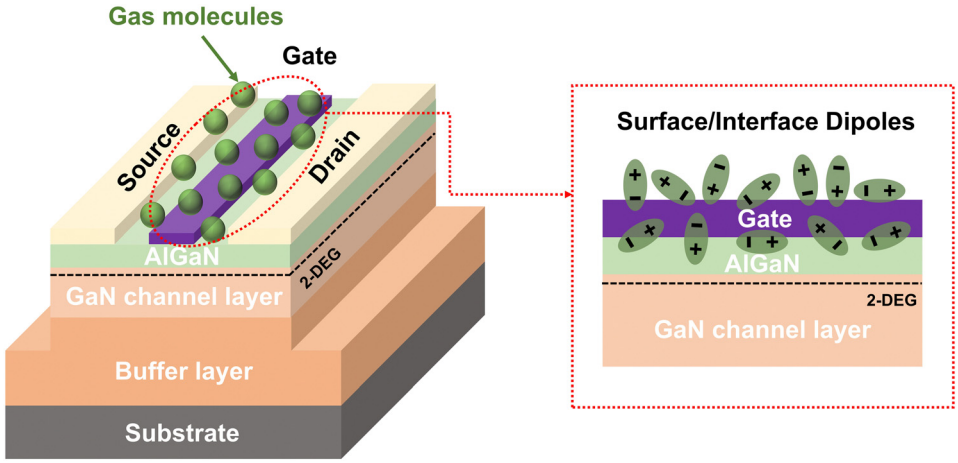

Fig. 6 Schematic illustration of the dipole-induced sensing mechanism. The chemisorption of target gas molecules induces potential variation due to surface and interface dipoles, subsequently affecting the current levels in the device upon detection.

sensors, and eqn (7) and (8) for HEMT sensors. This eliminates the difficulty of directly calculating the surface dipole potential, but the internal mechanism of GaN-based gas sensors involves the surface and interface dipoles must be clearly understood.

4.2. Thermodynamics of the gas adsorption model

Typically, gas adsorption onto solid surfaces follows the Langmuir adsorption model, which also applies to GaN-based gas sensors. Under steady-state conditions (the current reaching the saturation value (I_{max}), as shown in Fig. 5), the fraction of coverage (θ_i) of gas molecules on the surface of the sensing material can be expressed as:[74,79,153]

$$\theta_i = \frac{K_e\sqrt{P}}{1 + K_e\sqrt{P}} \tag{10}$$

where θ_i is the fractional interfacial coverage ranging from 0 to 1, K_e is the temperature and the concentration-dependent constant of the rate of effective equilibrium, and P is the partial pressure of the target gas, which can also be converted into gas concentration (ppm) according to $(P/P_{total}) \times 1\,000\,000$.

The adsorption of molecules of the target gas causes the Schottky barrier height variation ($\Delta\Phi_B$), where the adsorptive sites are mainly located on the surface and at the interface. Therefore, $\Delta\Phi_B$ can be considered to be proportional to the fraction of coverage θ_i:[32,74]

$$\Delta\Phi_B = \Delta\Phi_{B,max}\theta_i \tag{11}$$

where $\Delta\Phi_{B,max}$ is the maximum change in the Schottky barrier height. By combining eqn (3), (4) and (11), the Langmuir isotherm equation for Schottky diode sensors can be rewritten as:

$$\frac{1}{\ln\left(\frac{I_t}{I_0}\right)} = \frac{1}{\ln\left(\frac{I_{max}}{I_0}\right)} + \frac{1}{K_e\sqrt{P}\ln\left(\frac{I_{max}}{I_0}\right)} \tag{12}$$

where I_0 is the baseline current of the sensor without the presence of the sensing gas, I_{max} is the saturation current at a specific gas concentration, and I_t is the detection current at time t during the period of gas-sensing. By combining eqn (7), (8), and (11), the Langmuir isotherm equation of HEMT sensors can also be written as follows:

$$\frac{1}{\sqrt{I_t} - \sqrt{I_0}} = \frac{1}{\sqrt{I_{max}} - \sqrt{I_0}} + \frac{1}{K_e\sqrt{P}\left(\sqrt{I_{max}} - \sqrt{I_0}\right)} \tag{13}$$

To obtain the value of K_e, we can plot $1/\ln(I_t/I_0)$ *versus* $1/\sqrt{P}$ for diode sensors and $1/\sqrt{I_t} - \sqrt{I_0}$ *versus* $1/\sqrt{P}$ for HEMT sensors at a specific temperature. We can thus extract the temperature-dependent values of K_e, and then determine the adsorption enthalpy (ΔH°) and entropy (ΔS°) through the van't Hoff equation:[74,93,154]

$$\ln\left(K_e\sqrt{P}\right) = \frac{-\Delta H^\circ}{RT} + \frac{\Delta S^\circ}{R} \tag{14}$$

where ΔH° is the change in enthalpy, ΔS° is the change in entropy, R is the universal gas constant, and T is the absolute temperature. The value of ΔH° can be extracted from the slope of $\ln\left(K_e\sqrt{P}\right)$ *versus* T, and it indicates whether the thermodynamic process of gas adsorption is endothermic or exothermic. The value of ΔS°, which indicates the variation in disorder of the gas molecules after chemisorption, can be extracted from the intercept of the plot.

4.3. Kinetic analysis of gas adsorption and desorption

Temperature and gas concentrations play critical roles in both gas adsorption/desorption and related kinetics, and investigating their effects on the I–t characteristics provides valuable insights into device dynamic responses. The adsorption/desorption rates can be presented as differential equations with respect to time. With regard to the Langmuir adsorption isotherm, the kinetics of the transient characteristics of adsorption–desorption of the target gas on the surface of the sensing material can be expressed using the first-order equations shown below:[33,34]

$$\frac{d\theta_a(t)}{dt} = r_a\sqrt{P}(\theta_e - \theta_a(t)) \tag{15}$$

$$\frac{d\theta_d(t)}{dt} = -r_d\theta_d(t) \quad (16)$$

where the subscripts a, d, and e represent steady states of adsorption, desorption, and saturation, respectively, $d\theta_a(t)/dt$ and $d\theta_d(t)/dt$ are the reaction rates of adsorption and desorption of the gas, respectively, r_a and r_d are constants of the reaction rate, P is the partial pressure of the target gas, θ_e is the steady-state coverage fraction of saturation, and $\theta_a(t)$ and $\theta_d(t)$ are the time-dependent coverage fraction functions for gas adsorption and desorption, respectively. The surface of the sensing material is assumed to host several adsorption sites. The rate of adsorption $d\theta_a(t)/dt$ of the gas is assumed to be proportional to the fraction of available sites for the target gas to adsorb on the surface $(\theta_e - \theta_a(t))$, and to the partial pressure of the gas $\sqrt{P}$ according to eqn (15). The rate of desorption of the gas is assumed to be proportional to the fraction of already occupied sites $\theta_d(t)$ (eqn (16)). By solving the first-order differentiation equation, we can get[33]

$$\frac{\theta_a(t)}{\theta_e} = 1 - \exp\left(-r_a\sqrt{P}t\right) \quad (17)$$

$$\frac{\theta_d(t)}{\theta_e} = \exp(-r_d t) \quad (18)$$

Combing eqn (12) and (13), where we know that $\theta_a(t)$ and θ_e can be presented as $\ln\left(\frac{I_t}{I_0}\right)$ and $\ln\left(\frac{I_{max}}{I_0}\right)$, respectively, for the Schottky diode sensor. Eqn (17) and (18) can then be rewritten as

$$\frac{\theta_a(t)}{\theta_e} = \frac{\ln\left(\frac{I_t}{I_0}\right)}{\ln\left(\frac{I_{max}}{I_0}\right)} = 1 - \exp\left(-r_a\sqrt{P}t\right) \quad (19)$$

$$\frac{\theta_d(t)}{\theta_e} = \frac{\ln\left(\frac{I_t}{I_0}\right)}{\ln\left(\frac{I_{max}}{I_0}\right)} = \exp(-r_d t) \quad (20)$$

where I_t in eqn (19) and (20) is the detection current at time t as it rises and falls, respectively, as shown in Fig. 5. For HEMT sensors, we can rewrite the above equations as

$$\frac{\theta_a(t)}{\theta_e} = \frac{\sqrt{I_t} - \sqrt{I_0}}{\sqrt{I_{max}} - \sqrt{I_0}} = 1 - \exp\left(-r_a\sqrt{P}t\right) \quad (21)$$

$$\frac{\theta_d(t)}{\theta_e} = \frac{\sqrt{I_t} - \sqrt{I_0}}{\sqrt{I_{max}} - \sqrt{I_0}} = \exp(-r_d t) \quad (22)$$

We can reorganize eqn (19)–(22) to clearly show how to extract r_a and r_d:

$$\ln\left(1 - \frac{\ln\left(\frac{I_t}{I_0}\right)}{\ln\left(\frac{I_{max}}{I_0}\right)}\right) = -r_a\sqrt{P}t \quad (23)$$

$$\ln\left(\frac{\ln\left(\frac{I_t}{I_0}\right)}{\ln\left(\frac{I_{max}}{I_0}\right)}\right) = -r_d t \quad (24)$$

$$\ln\left(1 - \frac{\sqrt{I_t} - \sqrt{I_0}}{\sqrt{I_{max}} - \sqrt{I_0}}\right) = -r_a\sqrt{P}t \quad (25)$$

$$\ln\left(\frac{\sqrt{I_t} - \sqrt{I_0}}{\sqrt{I_{max}} - \sqrt{I_0}}\right) = -r_d t \quad (26)$$

By plotting $\ln\left(1 - \frac{\ln\left(\frac{I_t}{I_0}\right)}{\ln\left(\frac{I_{max}}{I_0}\right)}\right)$ and $\ln\left(\frac{\ln\left(\frac{I_t}{I_0}\right)}{\ln\left(\frac{I_{max}}{I_0}\right)}\right)$ *versus* t, we can extract r_a and r_d at different temperatures and gas concentrations, respectively, for Schottky diode sensors using eqn (23) and (24). The method to extract r_a and r_d for HEMT sensors is similar using eqn (25) and (26).

We can define the reaction time constants for adsorption and desorption (τ_a and τ_d) as

$$\tau_a = \frac{1}{r_a\sqrt{P}} \quad (27)$$

$$\tau_d = \frac{1}{r_d} \quad (28)$$

where r_a and r_d are the constants of reaction rates of adsorption and desorption, respectively. The Schottky diode and HEMT sensors have the same expressions for the reaction times for adsorption and desorption, and r_a and r_d can be obtained using eqn (23)–(28). Thus, the values of τ_a and τ_d can be obtained at different temperatures and gas concentrations.

Because the rates of adsorption and desorption are temperature dependent, we can calculate the activation energy (E_a) at different gas concentrations according to the Arrhenius equation based on the values of r_a and r_d.[33,93,134] The activation energy for the adsorption and desorption of the gas can be expressed as

$$\ln(r) = \ln(r_0) - \frac{E_a}{RT} \quad (29)$$

where r is the temperature-dependent rate constant that can be substituted with r_a and r_d to solve for the activation energy of adsorption and desorption, respectively. r_0 is the pre-exponential factor, E_a is the activation energy of gas for the adsorption and desorption, R is the universal gas constant, and T is the temperature. The activation energy is defined as the energy required to overcome the barrier of absorption and desorption of the gas molecules on the surface of the sensing material. The typical activation energy as a function of gas concentration is illustrated in Fig. 7, and is consistent with the results of previous publications.[32,33] The activation energies for adsorption and desorption have opposite signs (positive and negative, respectively). The energy of adsorption increases while that of desorption decreases with the increase in the

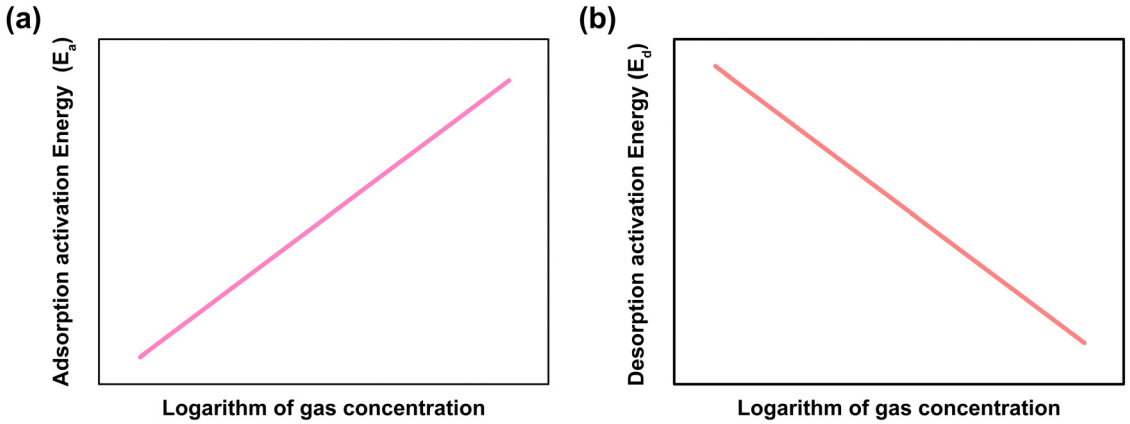

Fig. 7 The activation energy as a function of gas concentration: (a) adsorption and (b) desorption.

gas concentration. In general, the activation energy varies almost linearly with the logarithm of the gas concentration.

The above derivations rely on the transient response of the device at different temperatures and gas concentrations. The rate of absorption can also be presented as:[31,35,36]

$$r_a = \frac{P}{\sqrt{2\pi m k_B T}} S \exp\left(-\frac{E_a}{RT}\right) f(\theta) \quad (30)$$

where $\frac{P}{\sqrt{2\pi m k_B T}}$ is from the Hertz–Knudsen formula, and reveals the number of molecules striking a unit surface per unit time, m is the molar mass of the gas molecules, k_B is Boltzmann's constant, T is the temperature, S is the temperature-dependent sticking coefficient, E_a is the activation energy of absorption, R is the universal gas constant, and $f(\theta)$ specifies the fraction of the uncovered surface. The rate of desorption can be written as[36]

$$r_d = \nu \exp\left(-\frac{E_d}{RT}\right) \varphi(\theta) \quad (31)$$

where ν is the order-dependent pre-exponential constant, E_d is the activation energy of the desorption process, and $\varphi(\theta)$ specifies the fraction of the covered surface. At steady-state saturation, the rate of absorption is equal to that of desorption, and obeys the Langmuir isotherm equation. We can combine eqn (27), (28), (30) and (31) to obtain the final expressions of the reaction time constants of adsorption and desorption (τ_a and τ_d) as follows:

$$\tau_a = \frac{\sqrt{2\pi m k_B T}}{\sqrt[2]{P}} \frac{1}{S} \frac{1}{f(\theta)} \exp\left(\frac{E_a}{RT}\right) \quad (32)$$

$$\tau_d = \frac{1}{\nu} \frac{1}{\varphi(\theta)} \exp\left(\frac{E_d}{RT}\right) \quad (33)$$

The influence of the temperature T and the partial pressure of the target gas P (which can be converted into the gas concentration) on the characteristics of adsorption and desorption can be obtained from eqn (30)–(33). Fig. 8 depicts the relationships between r_a, r_d, τ_a, and τ_d, and the temperature and gas concentration according to eqn (30)–(33). When the temperature ranges from 300 K to 1500 K, the adsorption and desorption rates increase with the temperature as shown in Fig. 8(a) and (b). The same trends are shown in Fig. 8(c) and (d) at a fixed temperature of 300 K as the gas concentration is varied from 100 ppm to 1000 ppm. These results indicate that an increase in the temperature or the gas concentration accelerated the adsorption and desorption of the target gas on the surface of the sensing material. The corresponding experimental observations are discussed in the next section.

4.4. Factors influencing adsorption and desorption

Aforementioned theoretical equations elucidate the effect of temperature and gas concentration on adsorption and desorption. Some research studies have suggested that thinning down the AlGaN barrier enhances dynamic performance, but the exact reasons for this phenomenon remain unclear.[77,106,110] The gas adsorption and desorption, especially the trailing edge of the response curve (recovery time), are sensitive to the gas residence time. Therefore, the chamber size design and the gas flow rate setting play an important role in gas sensing test. By decreasing the chamber size or boosting the gas flow, gas residence time can be decreased, allowing faster gas adsorption and desorption. This modification theoretically improves the efficiency of the gas sensing system, which can further decrease the response and recovery times. Although research efforts have been made, more work needs to be performed to fully understand and consolidate the effects of these crucial variables. In this portion, we examine the impact of temperature and gas concentration on sensor performance through experimental observations and evaluate if the outcomes align with previously established theories.

4.4.1. The influence of temperature. Fig. 9 summarizes the response times (absorption time τ_a) and recovery times (desorption time τ_d) of different gas sensors as a function of temperature. Chen *et al.* developed a Pt nanoparticles (NPs)/Pt film-based H_2 sensor.[27] The transient behavior of the device was tested at an applied voltage of 0.4 V within a concentration range of H_2 from 1 ppm to 10 000 ppm and at a temperature ranging from 300 K to 523 K. The response time (τ_a) and recovery time (τ_d) were measured when the signal constituted

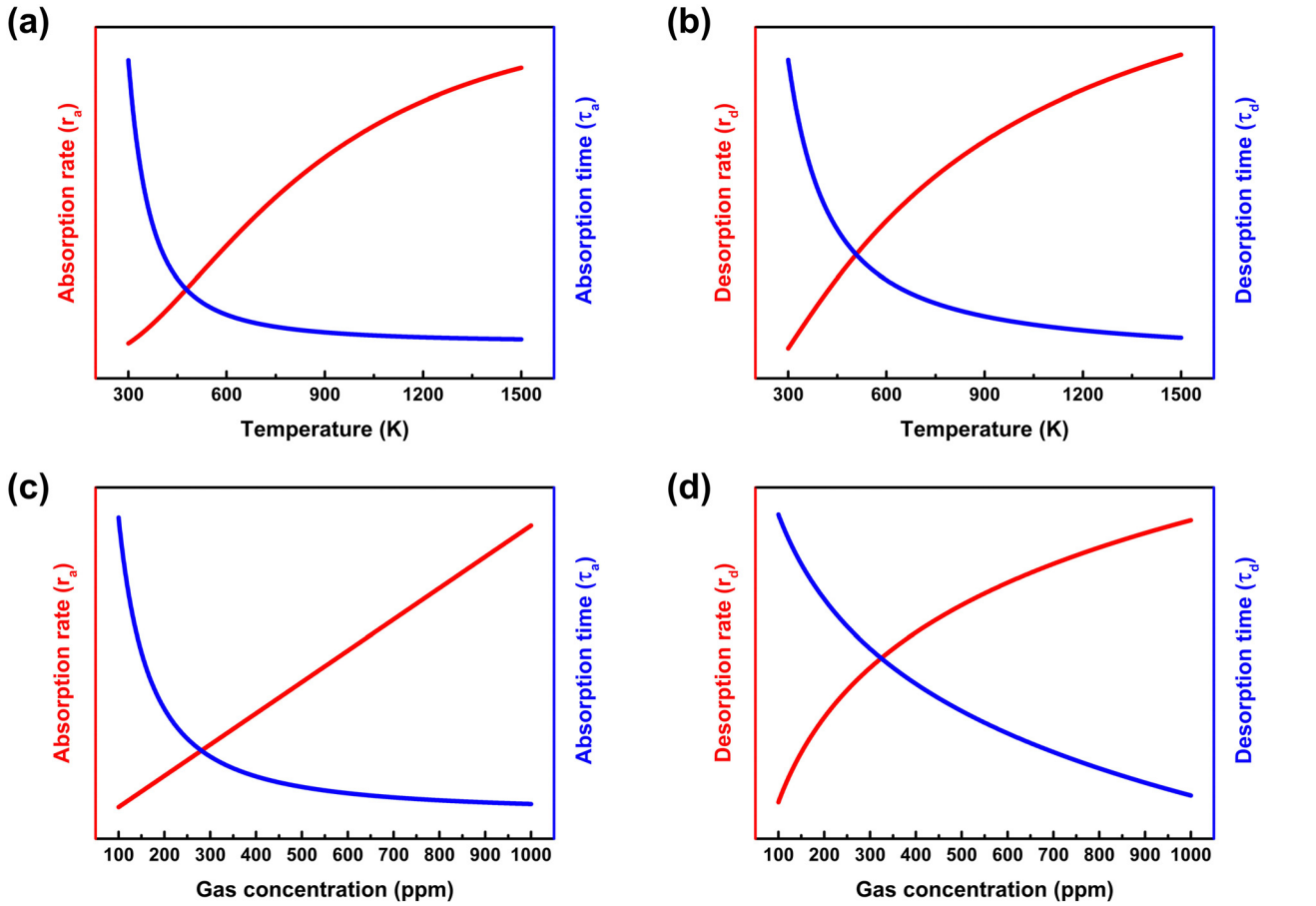

Fig. 8 Simplified illustration of the factors influencing the characteristics of adsorption and desorption of the gas (r_a, r_d, τ_a, and τ_d) according to eqn (30)–(33): (a) and (b) temperature *T*, (c) and (d) target gas concentration (recalculated from the partial pressure *P*).

90% of the overall response and recovery values (as shown in the insets of Fig. 9(a)). The values of τ_a and τ_d as a function of temperature in the above concentration range of H_2 are shown in Fig. 9(a). τ_a and τ_d decreased with the increase in temperature for all concentrations of H_2 gas. For example, τ_a decreased from 17 s to 3.2 s and τ_d decreased from 23 s to 5.8 s when the temperature rose from 300 K to 523 K when the concentration of H_2 was 10 000 ppm. Liu *et al.* fabricated a Pt/GaO_x-based NH_3 sensor by using hydrogen peroxide treatment and EP technology.[141] To evaluate the response of this NH_3 sensor, τ_a and τ_d were estimated through transient response experiments across varying concentrations (from 0.4 ppm to 1000 ppm) and temperatures (ranging from 300 K to 573 K). The results in Fig. 9(b) show that both τ_a and τ_d were lower at higher temperatures. When the temperature increased from 300 K to 573 K, τ_a decreased from 251 s to 86 s and τ_d decreased from 108 s to 15 s when the concentration of NH_3 was 1000 ppm. As seen in Fig. 9(a) and (b), the sensor exhibited improved dynamic performance when operated at higher temperatures. In order to better understand the impact of temperature, newer investigations examined two types of gas sensors: TiO_2 gate-based CO sensors proposed by Fan *et al.*[28] and Pt gate-based NO_2 sensors proposed by Ranjan *et al.*[29] As is shown in Fig. 9(c), the concentration of CO was fixed at 100 ppm. The response time decreased from 80 s to 4 s and the recovery time decreased from 200 s to 60 s when the temperature was increased from 210 °C to 300 °C. The enhanced responsiveness and accelerated recovery observed at elevated temperatures can be traced back to the increased formation of chemical equilibrium between adsorption and desorption processes. Likewise, the Pt-gate NO_2 gas sensor displayed a similar dependence on temperature, as illustrated in Fig. 9(d).[29] In the range of 30–300 °C at a constant concentration of 6 ppm NO_2, as temperature increases, the response and recovery times tend to decrease steadily. At higher temperatures, the improved dissociation, adsorption, and desorption of NO_2 onto the Pt surface led to a reduction in the response and recovery times.

The experimental setup shown in Fig. 9 was used to analyze the adsorption and desorption behavior of various gases interacting with diverse sensing substances. Increasing temperature generally results in a decline in their response and recovery times. These experimental data closely matched theoretical derivations (see Fig. 8(a) and (b)), thus confirming a substantial impact of temperature on the dynamics of GaN-based gas sensors. In summary, the shorter response and recovery times at higher temperatures might have been obtained owing to (1)

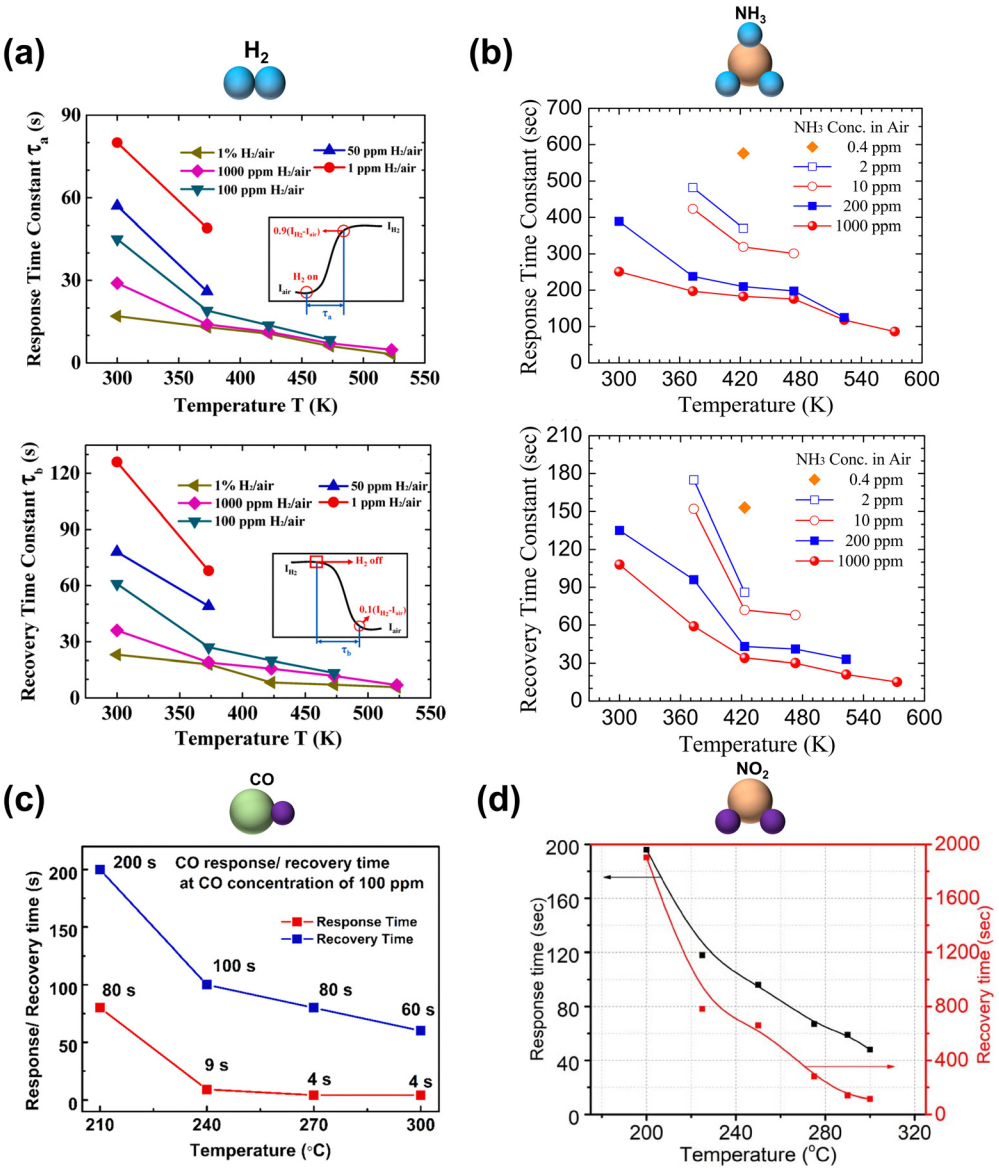

Fig. 9 Response and recovery times plotted against temperature for diverse gases interacting with different sensing materials provide insights into adsorption and desorption dynamics: (a) H_2 on Pt nanoparticles (NPs)/Pt films (reproduced from ref. 27 with permission from Elsevier. Copyright 2020, Elsevier).[27] (b) NH_3 on Pt/GaO_x (reproduced from ref. 141 with permission from the American Chemical Society. Copyright 2019, American Chemical Society).[141] (c) CO on TiO_2 (reproduced from ref. 28 with permission from Elsevier. Copyright 2022, Elsevier).[28] (d) NO_2 on Pt (reproduced from ref. 29 with permission from IOP Publishing. Copyright 2021, IOP Publishing).[29]

the faster adsorption and desorption of the gas according to eqn (30) and (31), (2) the collision of a larger number of gas molecules that enhanced the adsorption and desorption reactions, (3) the gas molecules receiving more thermal energy over a shorter time to overcome the activation energy, and (4) faster rates of dissociation and diffusion (only in the case of dissociation-induced absorption).

4.4.2. The influence of gas concentration. We inspected the experimental results of the changes in response and recovery times for various sensors with varying gas concentrations, as shown in Fig. 10. Liu *et al.* investigated the variations in response and recovery times of a Pt/GaO_x-based H_2 sensor with the temperature and gas concentration (Fig. 10(a)).[143] τ_a and τ_d were defined as the times needed to achieve 90% of the magnitudes of the overall response and recovery processes. They measured τ_a and τ_d *versus* temperature in a concentration range of H_2 gas from 1 ppm to 10 000 ppm under an applied voltage of 0.6 V. When the temperature was fixed at 300 K, the response and recovery times decreased with increasing H_2 concentration. For example, at 300 K, the values of τ_a of the proposed H_2 sensor were 74 s, 50 s, 42 s, 27 s, and 15 s under hydrogen concentrations of 1, 50, 100, 1000, and 10 000 ppm, respectively. The corresponding values of τ_d were 103 s, 60 s, 46 s, 30 s, and 19 s. The reduction in response and recovery times escalated across all temperature ranges (300–573 K) with an increase in gas concentration. A similar strategy was used to

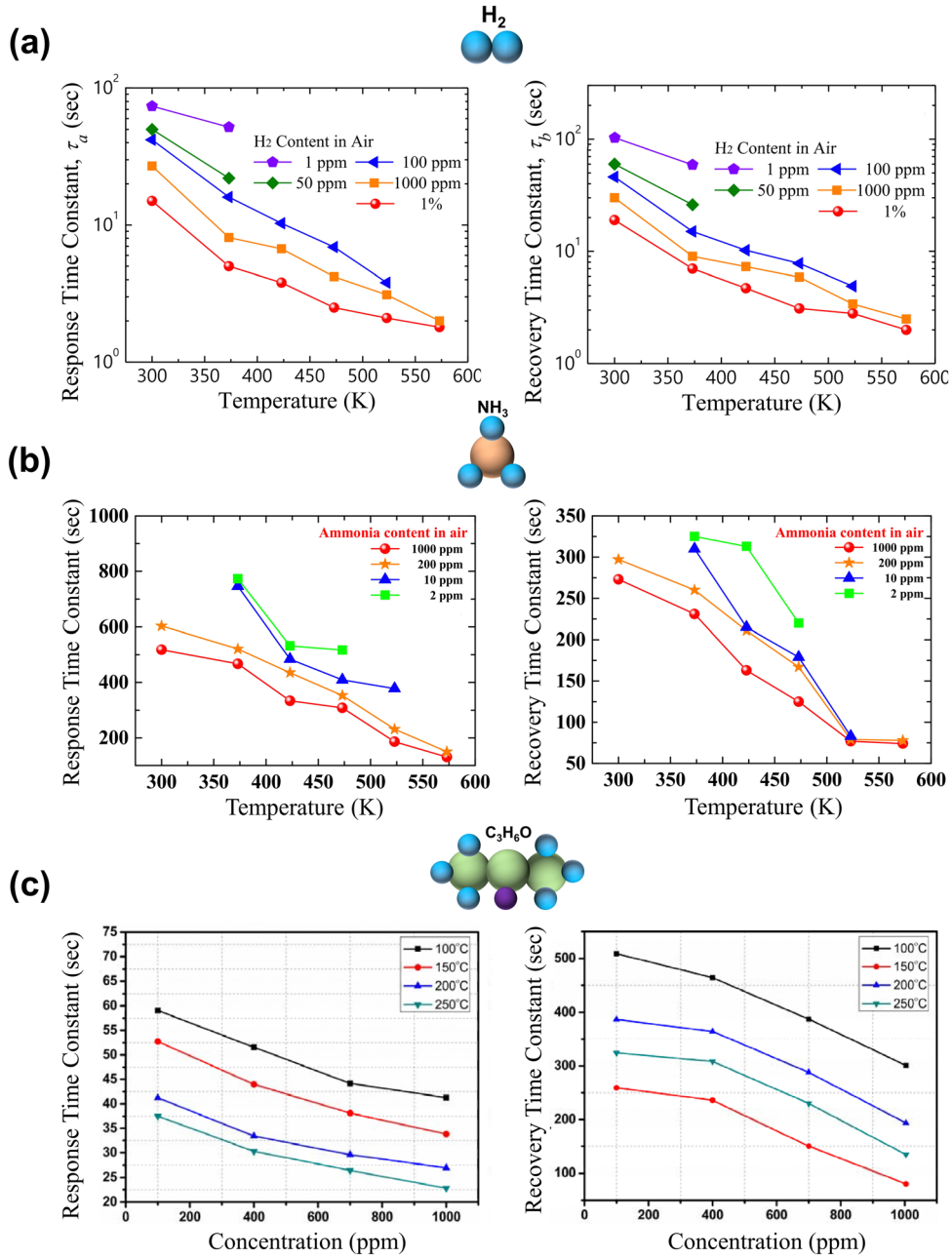

Fig. 10 Response and recovery times plotted against gas concentration for diverse gases interacting with different sensing materials provide insights into adsorption and desorption dynamics: (a) H_2 on Pt/GaO_x (reproduced from ref. 143 with permission from Elsevier. Copyright 2019, Elsevier).[143] (b) NH_3 on Pt nanoparticles (NPs)/Pt film (reproduced from ref. 46 with permission from IEEE. Copyright 2020, IEEE).[46] (c) Acetone on Pd (reproduced from ref. 33 with permission from IEEE. Copyright 2018, IEEE).[33]

assess the dynamic performance of devices in ref. 46. The values of τ_a and τ_d were obtained by using the same definition as mentioned above, over a range of temperatures from 300–573 K and concentrations of the NH_3 gas from 2–1000 ppm (Fig. 10(b)). τ_a and τ_d decreased from 517 s and 220 s to 308 s and 125 s, respectively, as the NH_3 concentration increased from 2 ppm to 1000 ppm at 473 K. In addition, a Pd-based acetone sensor was used to confirm that the increase in gas concentration reduces the response and recovery times of the sensor, as shown in Fig. 10(c).[33] The response and recovery times were plotted as a function of the concentration of acetone gas, and the results clearly showed that the values of τ_a and τ_d decreased monotonically with increasing concentration of acetone gas at all temperatures.

These above experiment results are in accordance with the qualitative analyses of the theoretical derivation (Fig. 8(c) and (d)), indicating that the concentration of gas is a crucial factor influencing the dynamic response of GaN-based gas sensors. A shorter response time can be attributed to the increase in gas concentration, which in turn increases the probability of

collisions of gas molecules increasing the rate of absorption, which is consistent with the description in eqn (30). Increasing the concentration of the gas likely increases the dissociation and diffusion coefficients, which in turn can enhance the absorption process. Furthermore, a shorter recovery time can be attributed to a higher fraction of surface coverage (θ_i) with high gas concentration, which shortened the reaction time to release the adsorbed gas molecules.

5. Application of dynamic responses

Recently, electronic noses (E-noses) and artificial olfaction systems (AOS) inspired by biological olfactory mechanisms have garnered significant attention due to their potential applications in fields like environmental monitoring, breath analysis, medical diagnosis, food quality control, and security. Two essential components in electronic nose/artificial olfaction systems for detecting both qualitative and quantitative aspects of diverse smells are a set of gas sensors array and data processing units. By emulating the functionality of olfactory receptors found within natural odor perception systems, the gas sensors array translates chemical stimuli into electrical impulses. Data processing units simulate the neural processing present in biological brains to examine, categorize, and recognize electrical signals produced by the array of gas sensors.

Multi-variable techniques enable identification of distinctive patterns or ''fingerprints'' specific to various types of gas samples. E-noses and AOS systems provide a simple and non-destructive technique for detecting different gases and their mixtures, and are capable of real-time monitoring.

Several efforts have been made to optimize the efficacy of E-nose and AOS devices through betterment of gas sensor precision, discernment, and long-term reliability, as previously discussed. Although gas sensor advancements play an important role, equally critical is the implementation of robust data analysis algorithms for handling multidimensional data, feature extraction, and accurately identifying complex gas combinations. For determining the composition of a gas sample, there exist two approaches: static responses and dynamic responses. In the case of static responses, the baseline state and saturation-related sensing response of the target gas are recorded for post processing (Fig. 11(a)). Dynamic responses include the shape of the curve of the transient response from the instance of injection of the gas to when the signal has been completely recovered with respect to the baseline (Fig. 11(b)).[155] Both strategies have their respective strengths and drawbacks when assessing the properties of a gas sample. The measurement of static responses requires more time for data acquisition for a quantitative analysis of the components of the gas mixture. In contrast, measurements of dynamic responses are less time consuming but require a higher frequency of sampling of the signals for a precise reconstruction of the response-related information of the sensor. In other words, higher frequency sampling yields more accurate representations of the dynamic behavior, albeit introducing challenges during subsequent data processing steps, whereas lower sampling rates could result in loss of vital information.[156] The study of dynamic responses supplies complementary details regarding the identity of the gas being analyzed since it captures valuable temporal characteristics.[157]

5.1. Gas feature extraction and optimization for electronic noses

The features of gas can be extracted from transient values (dynamic responses), steady-state values (static responses), or both. Dynamic responses often exhibit distinct behavioral signatures that distinguish between diverse gases/odors, providing more comprehensive insights compared to static signals alone.[158] Moreover, the use of the transient response reduces the time consumption for data acquisition. Therefore, feature extraction based on dynamic responses is a powerful method for the analysis and processing of sensing data. Brudzewski *et al.* applied principal component analysis (PCA) to extract the features of seven TGS sensors to determine their dynamic responses to odorous mixtures.[155] They obtained a 35D feature vector describing a single sample based on five parameters (relative amplitude, surface response, kurtosis, skewness, and full-width at half-maximum) from each TGS sensor of a seven-sensor array. The results showed that approximately 92% of the

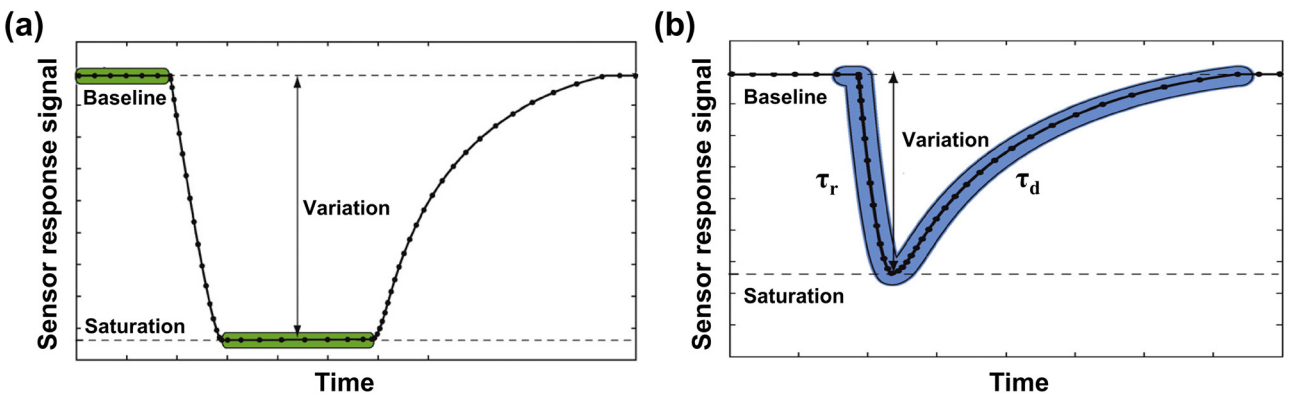

Fig. 11 Schematic illustration of two basic characteristics that enable the construction of the pattern of behavior of the gas: (a) static responses; (b) dynamic responses (reproduced from ref. 155 with permission from Elsevier. Copyright 2009, Elsevier).[155]

167 analyzed samples of ethanol and isopropanol were correctly classified based on the odor-related information present in the dynamic responses of the sensor. Distante *et al.* proposed a system to identify compound gases based on wavelet descriptors to analyze the transient responses of sensors at multiple resolutions.[157] Five tin oxide thin-film sensors were used to collect sensing-related information. Interactions among gas components and the sensor materials imprint unique kinetic patterns onto the transient signals generated by each device, yielding informational fingerprints specific to particular gas species present in the mixture. Hence, the major features of a specific gas could be obtained by analyzing the dynamic responses of the sensor. This method can be used to characterize and process multiple signals of odors based on the dynamic responses of an array of gas sensors. The period of signal recovery is more informative here than the rise period; a broader view encompassing the full transient response offers a more complete understanding of the odor profile.

In addition to extracting effective features of the gas from the dynamic responses of the sensor, selecting appropriate features, reducing their dimensions, and optimizing the recognition algorithm are equally important for applications of the electronic nose. The transient features of signals may contain meaningful information for gas sensors. For example, the recovery time is related to the type of sample gas.[157,159] The number of dimensions of the transient features may be very large, and feature selection algorithms such as forward selection,[159] sequential forward selection,[160] decision tree,[161] and max-pooling[162] are typically used to remove irrelevant and redundant features while maintaining the useful ones. By properly selecting a subset of the initially obtained transient features, the computational complexity of the recognition algorithm can be reduced and its accuracy can be improved.

Conventional algorithms for sensor array gases recognition lead to the loss of a large number of features of dynamic responses, hindering the attainment of optimal recognition precision. Therefore, Zhang *et al.* proposed a wavelet transform-based coefficient map-capsule network (WTCM-CapsNet) model to solve the problem of continuous selection and execution of the optimal algorithm to detect different gases in a dynamic environment.[163,164] This model uses the raw response signals from a sensor array without requiring any processing to extract the steady-state values of signals of the time domain as well as the maps of the wavelet coefficients of all dynamic response signals in the time–frequency domain as the input features. It can automatically learn the parameters for gas identification from the map of wavelet coefficients by using an iterative routing-by-agreement mechanism to yield an accuracy of approximately 100%. It is thus superior to conventional algorithms, such as the convolutional neural network (CNN; accuracy of 99.3%), K-nearest neighbor (KNN; 95.74%), support vector machine (SVM; 96.45%), random forest (95.74%), naive Bayesian classifier (92.91%), and backpropagation neural network (BPNN; 97.87%).[164]

5.2. Artificial olfactory system for in-sensor neuromorphic computing

Artificial olfactory systems emulate the function of the human olfactory system by combining sensor arrays and artificial intelligence, which have attracted a lot of attention and interest. Such systems endow a learnable agent with the ability to recognize and classify different odorous species after training. They show promising application prospects in IoT, such as food storage and industrial safety, monitoring the quality of indoor and outdoor air, and disease diagnosis. An in-sensor neuromorphic AOS features a high-level behavior of bio-creatures (*e.g.*, sensing, memory, inference, and decision) and energy efficiency. Emerging memristive devices can be leveraged in such systems owing to their simple structure, information processing in physics and integration facility.[165–168] The features of various patterns of gases need to be extracted from a gas sensor array and input into a neuromorphic computing system. The system is trained using the collected gas information, and then classifies gases based on a machine learning algorithm. The static responses of gases (*i.e.*, sensing responses) are widely used, but can only solve primitive problems like identifying a specific gas with a fixed concentration. The dynamic responses of sensors are more useful for complex empirical environments consisting of multiple gases with unpredictable concentrations as they contain more information on features of the gas than static responses.

Wang *et al.* proposed an artificial olfactory inference system by combining a dataset of two gases obtained from an array of sensors and memristive devices to show that rich features of the dynamic sensor responses improve the precision of classification in an environment containing multiple gases.[165] The transient responses of the sensor to 250 ppm CO and methane were collected from the dataset, as shown in Fig. 12(a). The dynamic and static features of the gases were extracted from the response speed of the sensor (50–70 s) and the period of its sensing response (100–120 s), respectively. Several sampling durations, such as 25%, 50%, 75% and the middle of the response speed and sensing response, were employed to reduce data overhead and redundancy, which could lower the power consumption and improve the efficiency of the inference system. The encoding process transformed the transient responses of the array of gas sensors into spike trains that could be efficiently processed by the memristive devices (Fig. 12(b)). To characterize the speed of response, the curves of transient response from 50 s to 70 s were sampled at an average of 0.2 s segments. The response speed was defined as the difference between neighboring segments. Once the response speed was above 1%, a spike was generated and was encoded into the spike trains. The average data from 100 s to 120 s of the sensing response were encoded into the frequency of the spike trains that obeyed the Poisson model. Because the sensing response of methane is higher than that of CO, more spikes were generated in its spike train (Fig. 12(b)). The schematic of this artificial olfactory inference system is shown in Fig. 12(c). A sensor array was used to collect raw data on transient responses to the environment. The encoded data were

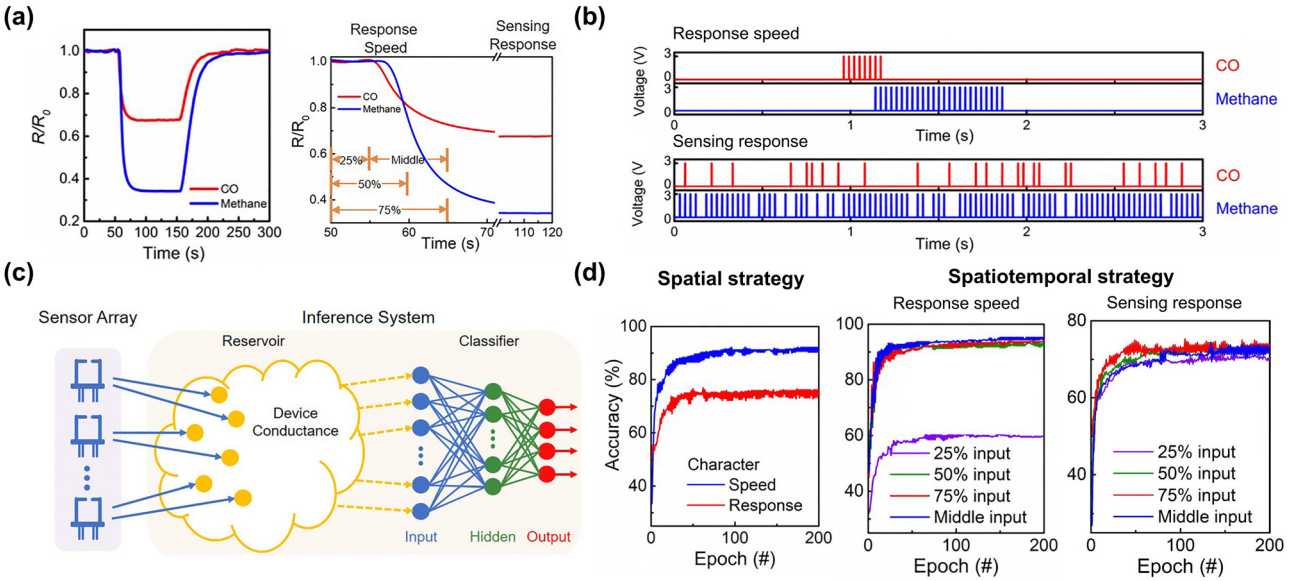

Fig. 12 An artificial olfactory inference system. (a) Curve of the normalized transient response of the gas sensor exposed to 250 ppm CO and methane. The schematic of the speed of response and period of sensing response with durations of partial sampling of the first 25%, 50%, 75%, and the middle time. (b) Encoded spike trains converted based on the speed of response and the sensing response. (c) Schematic diagram of an artificial olfactory inference system based on an RC system and a classifier, used to identify multiple gases. (d) Accuracy of classification using this olfactory inference system for samples based on spatial and spatiotemporal strategy (reproduced from ref. 165 with permission from Wiley. Copyright, 2021 Wiley)[165]

then input into a reservoir computing (RC) system based on volatile memristive devices to extract the relevant features. Finally, the neural network based on non-volatile memristive devices was used for inference and classification. To reduce the number of dimensions of the input features and the complexity of the classification system, a spatial strategy (only the response speed or the sensing response was used) and a spatiotemporal strategy (only a partial sampling of the response speed or the sensing response was chosen) were used. The results in Fig. 12(d) show that the response speed (dynamic features) yielded a higher accuracy of classification, of 92%, higher than the sensing response (static features), which had an accuracy of 75%. The result proves that the response speed extracted from the dynamic responses of the gas sensors contained more information than the sensing response obtained from their static responses, because the precision of classification improved. Moreover, the accuracy of classification of the duration of the partial sampling of the speed of response (accuracies of 92%, 94%, and 95% with 50%, 75%, and middle sampling duration, respectively) were higher than the sensing responses (accuracies of 72%, 74%, and 73% with 50%, 75%, and middle sampling duration, respectively). This showed that a higher recognition accuracy can be achieved by using the dynamic responses, which sufficiently certify the value and importance of the dynamic responses of gas sensors.

Han *et al.* developed an artificial olfactory system for an in-sensor neuromorphic nose by hybridizing a semiconductor metal–oxide (SMO) gas sensor and a single-transistor neuron composed of a MOSFET (Fig. 13(a)).[166] A biological olfactory system should be able to detect different odors and to encode them for in-sensor neuromorphic functioning. A spiking neural network (SNN) was employed to encode and analyze the complicated signals of mixed gases, as spike transmission is the main factor for reducing the power consumption of biological olfactory systems. The SMO gas sensor can detect odors in the environment and convert the gas-related signals to analog signals in the resistance mode. The electrical signals are then transported from the SMO gas sensor to the transistor through a metal inter-connection, where the transistor serves as a leaky integrate-and-fire (LIF) neuron to encode the signals into spike trains. When the input voltage from the SMO gas sensor on the drain electrode of the transistor is higher than a given threshold, spikes are fired at the output port, mimicking the spiking characteristics of the biological neuron. In addition, the gate electrode of the transistor can control the lateral inhibition of the artificial olfactory neuron to improve accuracy and energy efficiency by virtue of adaptation and distinctive signal contrast. The dynamic responses of the SMO gas sensor exposed to different target gases and concentrations are shown in Fig. 13(b). It shows a distinct gas-sensing response to different gases and concentrations. Since SnO_2 and WO_3 are n-type metal oxides, the resistance of the gas sensors decreased when exposed to reducing gases (NH_3, CO, and acetone) and increased when exposed to an oxidizing gas (NO_2). Fig. 13(c) shows two kinds of artificial olfactory neuron modules connected to the SnO_2 and WO_3 gas sensors. Four target gases (NH_3, CO, acetone, and NO_2) were used to verify their electrical characteristics. The spiking frequency f was modified according to the changes in the resistance of the dynamic responses of the gas sensors with various species of gases. The spiking frequency increased when the concentration of the reducing gases (NH_3, CO, and acetone) was increased (ON-type response), and

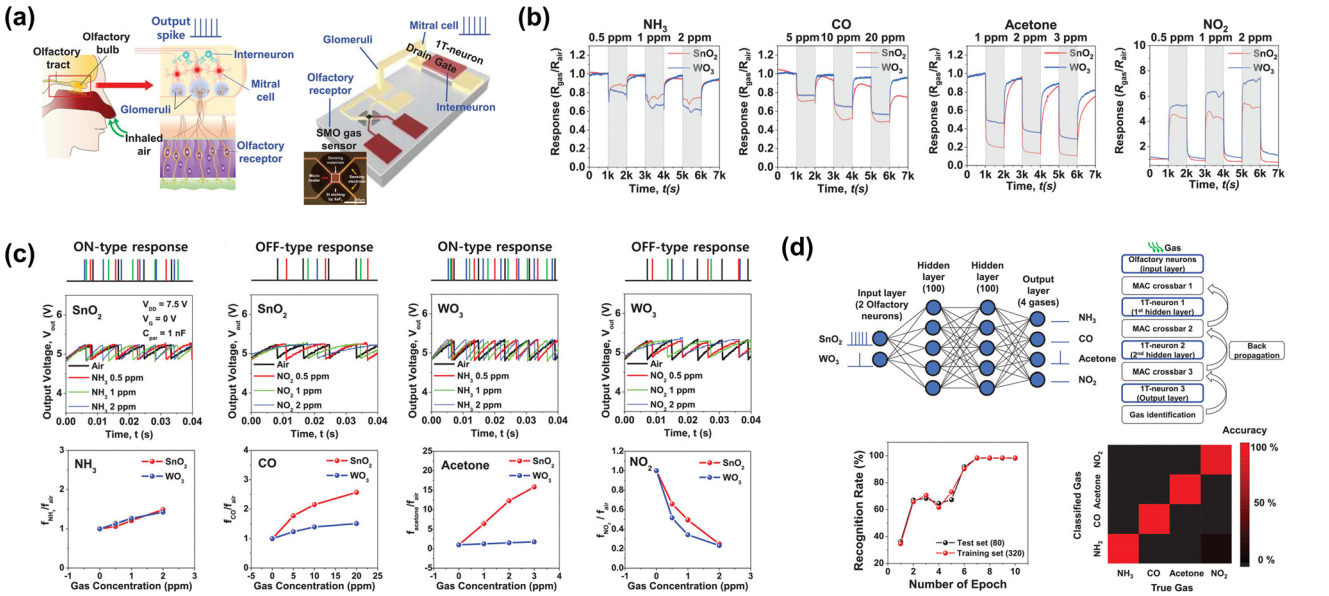

Fig. 13 Artificial olfactory neuron for an in-sensor neuromorphic nose. (a) A biological olfactory system and a SMO gas sensor with a MOSFET-based artificial olfactory neuron. (b) Dynamic responses of the SnO_2 and WO_3 gas sensors to four gas species—NH_3, CO, acetone, and NO_2—with varying concentrations. (c) Spiking characteristics of artificial olfactory neuronal modules. The spiking frequency f can be modified according to the changes in the resistance of the dynamic responses of the gas sensor with various species of gases. (d) Schematic of the multi-layer spiking neural network (SNN)and flowchart of the simulation, rate of recognition, and the results of the confusion matrix indicating the successful classification of four gases (reproduced from ref. 166 with permission from Wiley. Copyright, 2022 Wiley)[166]

decreased when the concentration of the oxidizing gas (NO_2) was increased (OFF-type response). This spiking frequency difference can be attributed to different chemical reactions between the gas species and the SMO gas sensor. These rich dynamic responses enabled the ON- and OFF-type responses of the olfactory neuron, making identification easier with a limited number of gas receptors and enhancing the efficiency of identification of the gas. The measured electrical properties of these artificial olfactory neuronal modules were used in simulations to classify four gases, as shown in Fig. 13(d). A four-layer SNN consisted of two input neurons, two hidden layers with 100 hidden neurons each, and four output neurons. The information of the gases was input into the input layer and the results of identification were exported at the output layer. The artificial olfactory neuronal modules attained an accuracy of gas identification of 98.25% after seven epochs. The confusion matrix of the results of classification of 80 test datasets confirmed these results. All four gas species had been accurately identified. Therefore, this artificial olfactory system is highly scalable and energy efficient, and offers promise for application in an in-sensor neuromorphic nose for classifying different species of gases in a mixture.

6. Discussion and outlook

6.1. Impact of the structure and fabrication on dynamic responses

Optimizing the layout of GaN-based gas sensors, especially the dimensions of the gate electrode, *i.e.*, its length (L_g) and width (W_g), directly impacts their dynamic responses. AlGaN/GaN-based sensors with gate electrodes of different W_g/L_g ratios (*e.g.*, 1, 5, 7, 10, and 100) have been demonstrateded.[84,95,96,108] Sokolovskij *et al.*[28,84] revealed that the dimensions of the gate electrode directly influence the sensitivity, current variations, and transient response of the sensor. As W_g/L_g was increased from 0.25 to 10, a 217% increase in the sensitivity and a 4630% increase in variations in the sensing current of the sensor were recorded under 500 ppm H_2. Moreover, its dynamic responses rate rose but its recovery rate slowed down as W_g/L_g was increased. For example, its response time decreased from 13.7 min to 5.7 min while its recovery time increased from 11.55 min to 25.65 min with increasing dimensions of the gate electrode. This provides a means of tuning the dynamic responses of the sensor to meet the requirements for sensing throughput and efficiency for various applications.

6.2. Post-signal processing

In the era of IoT, smart edge devices have imposed more stringent requirements on the capabilities of gas sensors to collect, transmit, and analyze data. The raw data are collected from gas sensors and transferred to a personal computer or the cloud. With numerous and different gas sensors involved in detecting the intended gas, there is an increase in the amount of sensing data, leading to large data transfer overhead and energy consumption. From the perspective of software, several post-signal processing techniques have been proposed to reduce the amount of redundant data and reduce errors in the responses of the sensor. Liu *et al.*[150] and Hsu *et al.*[101] reported reductions in the data of 64.22% and 97%, respectively, by using the polynomial difference recovery (GPDR) model.

Post-processing data can also be recovered accurately through applying this model. The Kalman algorithm and the shaped-preserving piecewise cubic interpolation (SPPCI) algorithm also helps to reduce the amount of redundant data and recover the original signal after transmission while yielding a small error in the responses of the sensor.[46,114,145] From the perspective of hardware, it is important to improve the dynamic responses of the gas sensor. A fast response and recovery facilitate efficient sensing and reduce redundancy in the data, energy consumption, and the cost of data transmission. Hence, the theoretical and experimental methods summarized in this review may benefit wireless sensors and the underlying IoT applications.

6.3. Outlook

GaN-based devices constructed from suitably chosen materials possess great promise in addressing existing challenges faced by conventional Si-based devices, and have made notable contributions towards advancing gas sensing technology. In this review, we discussed and summarized progress in research on GaN-based gas sensors for the identification of gases and chemical compounds, such as hydrogen (H_2), hydrogen sulfide (H_2S), ammonia (NH_3), methane (CH_4), nitric oxide (NO), nitrogen dioxide (NO_2), carbon monoxide (CO), carbon dioxide (CO_2), oxygen (O_2), and acetone. A comprehensive evaluation of distinct sensing performance of different gas sensors was provided in terms of their range of detection, optimized operating temperature, and response and recovery times. We also examined common approaches employed during the fabrication of GaN-based gas sensors. Moreover, we detailed the dynamic responses of GaN-based gas sensors. We comprehensively discussed their sensing mechanism as well as the characteristics of dynamic adsorption and desorption of gases, providing a different perspective for surveying this field in comparison to the existing literature. Systematic assessments revealed that both response time and recovery time decreased with rising gas concentrations and temperatures. Furthermore, the significance and potential of utilizing the dynamic responses of the sensor within electronic noses and artificial olfactive systems were explored to emphasize their value and applicability in such systems. Additionally, the influences of structural design and fabrication processes on dynamic responses and subsequent signal processing were analyzed.

In summary, gas-sensing technology is becoming increasingly important in environmental monitoring, medical diagnostics, and industrial safety. GaN-based gas sensors are a promising candidate for such applications which are part of the IoTs in the form of smart environments and smart homes.[169–171] They meet the requirements of ultra-low power consumption, low cost, long lifetime, integration into electronic circuits, and small size such that they can be used for remote monitoring and in enhanced automated systems. Despite the potential benefits, there still remain obstacles in optimizing the performance and understanding the underlying mechanisms of these sensors. The sensitivity, selectivity, and the speeds of response and recovery of the sensor need to be improved to meet the desired requirements. The performance of the sensor is also significantly influenced by factors such as inter-electrode spacing, quantity of electrodes, and surface area devoted to sensing.[172] In-depth investigations into miniature gas sensor characteristics could greatly aid the integration of GaN-based gas sensors into advanced IoT frameworks. Although much attention has been devoted to studying how temperature and concentration affect the sensor's dynamic responses, other variables like the shape and depth of the barrier recess and the geometry design of the gate electrode have received less scrutiny. A systematic theoretical framework is needed to provide guidance for designing the sensor, improving its performance, and orientating its application because tunable dynamic responses provide room for higher data throughput and efficiency as well as better post-processing of the signals. Moreover, promising opportunities exist for employing the sensor's intricate dynamic responses in E-nose and AOS applications. Mining the values of the dynamic responses of the sensor and developing associated algorithms should be considered in future works in this area. From the perspective of application, most experiments on gas sensing are largely based on ideal laboratory conditions rather than real-world environments. The sensitivity of GaN-based sensors in particular decreases significantly in the presence of humidity, which limits their scope of application. Therefore, comprehensive real-world field testing is needed to ensure that the sensor is effective. Research is also needed to address critical issues like device scalability, reproducibility, and reliability. Furthermore, owing to their chemical and physical stability, optical transparency, biocompatibility, and sustainability, the new generation of GaN-based sensors is promising for use in applications involving the detection of gases, liquids, biochemicals, pressure, ultraviolet light, and stress and strain. The development of lightweight, compact, and wearable GaN-based sensors is also expected. These innovations will have a long-term impact on significant areas of research and application, such as defense, space exploration, agriculture, healthcare, productivity, and environmental monitoring. We hope that the exhaustive literature appraisal and theoretical discourse in this review will help the reader better understand the dynamic responses of GaN-based gas sensors, and will assist in accelerating and fostering their development and adoption across various applications.

Author contributions

Yang Jiang (conceptualization, investigation, methodology, validation, visualization, and writing – original draft), Wenmao Li (formal analysis and validation), Fangzhou Du (formal analysis and visualization), Robert Sokolovskij (formal analysis and writing – review and editing), Yi Zhang (investigation), Shuhui Shi (visualization), Weiguo Huang (writing – review and editing), Qing Wang (writing – review and editing, project administration, supervision, and funding acquisition), Hongyu Yu (writing – review and editing, project administration, supervision, and funding acquisition) and Zhongrui Wang (writing – review and editing, project administration, supervision, and funding acquisition).

Conflicts of interest

There are no conflicts to declare.

Acknowledgements

This research was supported by the National Key R&D Program of China (grant no. 2018YFA0701500), the National Natural Science Foundation of China (grant no. 62122004, 61874138, 61888102, 61821091, and 62274082), the Strategic Priority Research Program of the Chinese Academy of Sciences (grant no. XDB44000000), the Hong Kong Research Grant Council (grant no. 27206321 and 17205922), the Innovation and Technology Commission of Hong Kong (grant no. MHP/066/20), the research on mechanism of source/drain Ohmic contact and the related GaN p-FET (grant no. 2023A1515030034), research on the fabrication and mechanism of GaN power and RF devices (grant no. JCYJ20200109141233476), research on the GaN chip for 5G Applications (grant no. JCYJ20210324120409025), research on highly reliable GaN power devices and the related industrial power system (grant no. HZQB-KCZYZ-2021052), the study on the reliability of GaN power devices (grant no. JCYJ20220818100605012), the Shenzhen Science and Technology Program (grant no. JSGG20220831094404008), and research on novelty low-resistance source/drain Ohmic contact for GaN p-FET (grant no. JCYJ20220530115411025). This research is also partially supported by the ACCESS-AI Chip Center for Emerging Smart Systems, sponsored by the Innovation and Technology Fund (ITF), Hong Kong SAR.

References

1 A. Dey, *Mater. Sci. Eng. B*, 2018, **229**, 206–217.
2 C. Wang, L. Yin, L. Zhang, D. Xiang and R. Gao, *Sensors*, 2010, **10**, 2088–2106.
3 M. V. Nikolic, V. Milovanovic, Z. Z. Vasiljevic and Z. Stamenkovic, *Sensors*, 2020, **20**, 6694.
4 S. Hong, M. Wu, Y. Hong, Y. Jeong, G. Jung, W. Shin, J. Park, D. Kim, D. Jang and J.-H. Lee, *Sens. Actuators, B*, 2021, **330**, 129240.
5 F. Shoucair, *IEEE Trans. Compon., Hybrids, Manuf. Technol.*, 1989, **12**, 780–788.
6 C.-F. Lo, Y. Xi, L. Liu, S. J. Pearton, S. Doré, C.-H. Hsu, A. M. Dabiran, P. P. Chow and F. Ren, *Sens. Actuators, B*, 2013, **176**, 708–712.
7 E. A. Jones, F. Wang and B. Ozpineci, Application-based review of GaN HFETs, *2014 IEEE Workshop on Wide Bandgap Power Devices and Applications*, IEEE, 2014.
8 T. Mizutani, M. Ito, S. Kishimoto and F. Nakamura, *IEEE Electron Device Lett.*, 2007, **28**, 549–551.
9 F. Iucolano and T. Boles, *Mater. Sci. Semicond. Process.*, 2019, **98**, 100–105.
10 S. Pearton, F. Ren, Y.-L. Wang, B. Chu, K. Chen, C. Chang, W. Lim, J. Lin and D. Norton, *Prog. Mater. Sci.*, 2010, **55**, 1–59.
11 S. Pearton, B. Kang, S. Kim, F. Ren, B. Gila, C. Abernathy, J. Lin and S. Chu, *J. Phys.: Condens. Matter*, 2004, **16**, R961.
12 K. T. Upadhyay and M. K. Chattopadhyay, *Mater. Sci. Eng. B*, 2021, **263**, 114849.
13 J. Ajayan, D. Nirmal, R. Ramesh, S. Bhattacharya, S. Tayal, L. L. Joseph, L. R. Thoutam and D. Ajitha, *Measurement*, 2021, **186**, 110100.
14 N. Sharma, V. Pandey, A. Gupta, S. T. Tan, T. Sudhiranjan and M. Kumar, *J. Mater. Chem. C*, 2022, **10**, 12157–12190.
15 D. Segev and C. G. Van de Walle, *EPL*, 2006, **76**, 305.
16 S. Heikman, S. Keller, Y. Wu, J. S. Speck, S. P. DenBaars and U. K. Mishra, *J. Appl. Phys.*, 2003, **93**, 10114–10118.
17 R. Quay, *Gallium Nitride Electronics*, 2008, 311–336.
18 M. Meneghini, G. Meneghesso and E. Zanoni, *Power GaN Devices-Materials, Applications and Reliability*, Springer International Publishing, Cham, 2017.
19 O. Ambacher, J. Smart, J. Shealy, N. Weimann, K. Chu, M. Murphy, W. Schaff, L. Eastman, R. Dimitrov and L. Wittmer, *J. Appl. Phys.*, 1999, **85**, 3222–3233.
20 O. Ambacher, B. Foutz, J. Smart, J. Shealy, N. Weimann, K. Chu, M. Murphy, A. Sierakowski, W. Schaff and L. Eastman, *J. Appl. Phys.*, 2000, **87**, 334–344.
21 E. Yu, X. Dang, P. Asbeck, S. Lau and G. Sullivan, *J. Vac. Sci. Technol., B: Microelectron. Nanometer Struct.--Process., Meas., Phenom.*, 1999, **17**, 1742–1749.
22 B. H. Morkoc, S. Strite, G. Gao, M. Lin, B. Sverdlov and M. Burns, *J. Appl. Phys.*, 1994, **76**, 1363–1398.
23 R. S. Pengelly, S. M. Wood, J. W. Milligan, S. T. Sheppard and W. L. Pribble, *IEEE Trans. Microwave Theory Tech.*, 2012, **60**, 1764–1783.
24 S. N. S. Nakamura, *Jpn. J. Appl. Phys.*, 1991, **30**, L1705.
25 J. Ohta, H. Fujioka, M. Oshima, K. Fujiwara and A. Ishii, *Appl. Phys. Lett.*, 2003, **83**, 3075–3077.
26 A. Kadir, S. Srivastava, Z. Li, K. E. K. Lee, W. A. Sasangka, S. Gradecak, S. J. Chua and E. A. Fitzgerald, *Thin Solid Films*, 2018, **663**, 73–78.
27 W.-C. Chen, J.-S. Niu, I.-P. Liu, B.-Y. Ke, S.-Y. Cheng and W.-C. Liu, *Sens. Actuators, B*, 2021, **331**, 129320.
28 M.-Y. Fan, R. Sokolovskij, Q. Wang, H. Zheng, K. Wen, F. Du, G. Zhou, Y.-L. Jiang and H. Yu, *Sens. Actuators, B*, 2022, **359**, 131556.
29 A. Ranjan, R. Lingaparthi, N. Dharmarasu and K. Radhakrishnan, *J. Electrochem. Soc.*, 2021, **168**, 047502.
30 I.-P. Liu, C.-H. Chang, B.-Y. Ke and K.-W. Lin, *IEEE Sens. J.*, 2019, **19**, 10207–10213.
31 K. Laidler, S. Glasstone and H. Eyring, *J. Chem. Phys.*, 1940, **8**, 659–667.
32 J. Song and W. Lu, *IEEE Sens. J.*, 2008, **8**, 903–909.
33 Acetone Adsorption Characteristics of Pd/AlGaN/GaN Heterostructure Grown by PAMBE: A Kinetic Interpretation at Low Temperature, in *2018 IEEE Sensors*, 18329531.
34 M. J. Pilling and P. W. Seakins, *Reaction kinetics*, Oxford University Press, 1995.
35 H. Okada, A. Naruse, Y. Furukawa and A. Wakahara, *Jpn. J. Appl. Phys.*, 2011, **50**, 01AD08.
36 R. Schlögl, *Angew. Chem., Int. Ed.*, 2015, **54**, 3465–3520.

37 B. Luther, S. Wolter and S. Mohney, *Sens. Actuators, B*, 1999, **56**, 164–168.
38 J. Schalwig, G. Müller, O. Ambacher and M. Stutzmann, *Phys. Status Solidi A*, 2001, **185**, 39–45.
39 B. Kang, F. Ren, B. Gila, C. Abernathy and S. Pearton, *Appl. Phys. Lett.*, 2004, **84**, 1123–1125.
40 B. Kang, R. Mehandru, S. Kim, F. Ren, R. Fitch, J. Gillespie, N. Moser, G. Jessen, T. Jenkins and R. Dettmer, *Appl. Phys. Lett.*, 2004, **84**, 4635–4637.
41 J.-R. Huang, W.-C. Hsu, Y.-J. Chen, T.-B. Wang, H.-I. Chen and W.-C. Liu, *IEEE Sens. J.*, 2010, **11**, 1194–1200.
42 H.-I. Chen, Y.-C. Cheng, C.-H. Chang, W.-C. Chen, I.-P. Liu, K.-W. Lin and W.-C. Liu, *Sens. Actuators, B*, 2017, **247**, 514–519.
43 Y.-Y. Tsai, K.-W. Lin, C.-T. Lu, H.-I. Chen, H.-M. Chuang, C.-Y. Chen, C.-C. Cheng and W.-C. Liu, *IEEE Trans. Electron Devices*, 2003, **50**, 2532–2539.
44 B. Kang, S. Kim, F. Ren, B. Gila, C. Abernathy and S. Pearton, *Sens. Actuators, B*, 2005, **104**, 232–236.
45 J.-F. Xiao, C.-P. Hsu and Y.-L. Wang, *ECS Trans.*, 2015, **66**, 159.
46 C.-H. Chang, W.-C. Chen, J.-S. Niu, B.-Y. Ke, S.-Y. Cheng, K.-W. Lin and W.-C. Liu, *IEEE Trans. Electron Devices*, 2019, **67**, 296–303.
47 Y. Xi, L. Liu, F. Ren, S. J. Pearton, J. Kim, A. Dabiran and P. P. Chow, *J. Vac. Sci. Technol., B: Nanotechnol. Microelectron.: Mater., Process., Meas., Phenom.*, 2013, **31**, 032203.
48 S. Das, S. Ghosh, R. Kumar, A. Bag and D. Biswas, *IEEE Trans. Electron Devices*, 2017, **64**, 4650–4656.
49 C. Bishop, J.-P. Salvestrini, Y. Halfaya, S. Sundaram, Y. El Gmili, L. Pradere, J. Y. Marteau, M. Assouar, P. Voss and A. Ougazzaden, *Appl. Phys. Lett.*, 2015, **106**, 243504.
50 M. Ali, V. Cimalla, V. Lebedev, H. Romanus, V. Tilak, D. Merfeld, P. Sandvik and O. Ambacher, *Sens. Actuators, B*, 2006, **113**, 797–804.
51 T.-H. Tsai, H.-I. Chen, I.-P. Liu, C.-W. Hung, T.-P. Chen, L.-Y. Chen, Y.-J. Liu and W.-C. Liu, *IEEE Trans. Electron Devices*, 2008, **55**, 3575–3581.
52 T.-Y. Chen, H.-I. Chen, C.-C. Huang, C.-S. Hsu, P.-S. Chiu, P.-C. Chou, R.-C. Liu and W.-C. Liu, *IEEE Trans. Electron Devices*, 2011, **58**, 4079–4086.
53 J.-R. Huang, W.-C. Hsu, Y.-J. Chen, T.-B. Wang, K.-W. Lin, H.-I. Chen and W.-C. Liu, *Sens. Actuators, B*, 2006, **117**, 151–158.
54 G. Chen, A. H. W. Choi, P. T. Lai and W. M. Tang, *J. Vac. Sci. Technol., B: Nanotechnol. Microelectron.: Mater., Process., Meas., Phenom.*, 2014, **32**, 011212.
55 H. Kim, W. Lim, J.-H. Lee, S. Pearton, F. Ren and S. Jang, *Sens. Actuators, B*, 2012, **164**, 64–68.
56 K. H. Baik, S. Jung, C.-Y. Cho, K.-H. Park, F. Ren, S. J. Pearton and S. Jang, *Sens. Actuators, B*, 2020, **317**, 128234.
57 P.-C. Chou, H.-I. Chen, I.-P. Liu, W.-C. Chen, C.-C. Chen, J.-K. Liou, C.-J. Lai and W.-C. Liu, *Int. J. Hydrogen Energy*, 2015, **40**, 9006–9012.
58 J. Song, W. Lu, J. S. Flynn and G. R. Brandes, *Appl. Phys. Lett.*, 2005, **87**, 133501.
59 J. Song, W. Lu, J. S. Flynn and G. R. Brandes, *Solid-State Electron.*, 2005, **49**, 1330–1334.
60 S. Jung, K. H. Baik, F. Ren, S. J. Pearton and S. Jang, *IEEE Electron Device Lett.*, 2017, **38**, 657–660.
61 S. Jung, K. H. Baik, F. Ren, S. J. Pearton and S. Jang, *IEEE Sens. J.*, 2017, **17**, 5817–5822.
62 Y. Xi, L. Liu, Y.-H. Hwang, O. Phillips, F. Ren, S. J. Pearton, J. Kim, C.-H. Hsu, C.-F. Lo and J. Wayne Johnson, *J. Vac. Sci. Technol., B: Nanotechnol. Microelectron.: Mater., Process., Meas., Phenom.*, 2013, **31**, 032202.
63 T.-Y. Chen, H.-I. Chen, P.-S. Chiu, C.-C. Huang, C.-S. Hsu, P.-C. Chou, R.-C. Liu and W.-C. Liu, *Mater. Chem. Phys.*, 2012, **135**, 150–157.
64 S.-Y. Chiu, H.-W. Huang, K.-C. Liang, T.-H. Huang, K.-P. Liu, J.-H. Tsai and W.-S. Lour, *Semicond. Sci. Technol.*, 2009, **24**, 045007.
65 T.-Y. Chen, H.-I. Chen, C.-S. Hsu, C.-C. Huang, C.-F. Chang, P.-C. Chou and W.-C. Liu, *IEEE Electron Device Lett.*, 2012, **33**, 612–614.
66 C.-S. Hsu, K.-W. Lin and W.-C. Liu, *J. Electrochem. Soc.*, 2013, **160**, B139.
67 J.-F. Xiao, C.-P. Hsu, I. Sarangadharan, G.-Y. Lee, J.-I. Chyi and Y.-L. Wang, *ECS J. Solid State Sci. Technol.*, 2016, **5**, Q137.
68 P.-C. Chou, H.-I. Chen, I.-P. Liu, C.-W. Hung, C.-C. Chen, J.-K. Liou and W.-C. Liu, *Sens. Actuators, B*, 2014, **203**, 258–262.
69 T.-Y. Chen, H.-I. Chen, Y.-J. Liu, C.-C. Huang, C.-S. Hsu, C.-F. Chang and W.-C. Liu, *Sens. Actuators, B*, 2011, **155**, 347–350.
70 T.-Y. Chen, H.-I. Chen, Y.-J. Liu, C.-C. Huang, C.-S. Hsu, C.-F. Chang and W.-C. Liu, *IEEE Trans. Electron Devices*, 2011, **58**, 1541–1547.
71 S. Jung, K. H. Baik, F. Ren, S. Pearton and S. Jang, *ECS J. Solid State Sci. Technol.*, 2018, **7**, Q3020.
72 A. Hudeish, A. A. Aziz, Z. Hassan, C. Tan, H. A. Hassan and K. Ibrahim, High-temperature Pt Schottky barrier gas sensor on p-type GaN, in *2005 Asian Conference on Sensors and the International Conference on New Techniques in Pharmaceutical and Biomedical Research*, 8672060, 2005.
73 V. Popa, I. Tiginyanu, V. Ursaki, O. Volcius and H. Morkoç, *Semicond. Sci. Technol.*, 2006, **21**, 1518.
74 S. Das, S. Majumdar, R. Kumar, S. Ghosh and D. Biswas, *Scr. Mater.*, 2016, **113**, 39–42.
75 S. Das, A. Bag, R. Kumar and D. Biswas, *IEEE Electron Device Lett.*, 2017, **38**, 383–386.
76 J. Sun, R. Sokolovskij, E. Iervolino, F. Santagata, Z. Liu, P. M. Sarro and G. Zhang, *IEEE Trans. Electron Devices*, 2019, **66**, 4373–4379.
77 J. Sun, T. Zhan, R. Sokolovskij, Z. Liu, P. M. Sarro and G. Zhang, *IEEE Sens. J.*, 2021, **21**, 16475–16483.
78 J. Sun, R. Sokolovskij, E. Iervolino, Z. Liu, P. M. Sarro and G. Zhang, *J. Microelectromech. Syst.*, 2019, **28**, 997–1004.
79 C. Bishop, Y. Halfaya, A. Soltani, S. Sundaram, X. Li, J. Streque, Y. El Gmili, P. L. Voss, J. P. Salvestrini and A. Ougazzaden, *IEEE Sens. J.*, 2016, **16**, 6828–6838.

80 M. Eickhoff, J. Schalwig, G. Steinhoff, O. Weidemann, L. Görgens, R. Neuberger, M. Hermann, B. Baur, G. Müller and O. Ambacher, *Phys. Status Solidi C*, 2003, 1908–1918.
81 J. H. Choi, M. G. Jo, S. W. Han, H. Kim, S. H. Kim, S. Jang, J. S. Kim and H. Y. Cha, *Electron. Lett.*, 2017, **53**, 1200–1202.
82 J. Zhang, R. Sokolovskij, G. Chen, Y. Zhu, Y. Qi, X. Lin, W. Li, G. Q. Zhang, Y.-L. Jiang and H. Yu, *Sens. Actuators, B*, 2019, **280**, 138–143.
83 R. Sokolovskij, J. Zhang, E. Iervolino, C. Zhao, F. Santagata, F. Wang, H. Yu, P. M. Sarro and G. Q. Zhang, *Sens. Actuators, B*, 2018, **274**, 636–644.
84 R. Sokolovskij, E. Iervolino, C. Zhao, F. Wang, H. Yu, F. Santagata, P. M. Sarro and G. Q. Zhang, Pt-AlGaN/GaN HEMT-sensor layout optimization for enhancement of hydrogen detection, in *2017 IEEE Sensors*, 17467338, 2017.
85 A. Watanabe, S. Nakamura and T. Okumura, Selective hydrogen detection of Pd/AlGaN/GaN HEMT-type sensors by temperature sweep operation, in *2012 IEEE Sensor*, 13256383, 2012.
86 S. Jung, K. H. Baik, F. Ren, S. J. Pearton and S. Jang, *J. Vac. Sci. Technol., B: Nanotechnol. Microelectron.: Mater., Process., Meas., Phenom.*, 2017, **35**, 042201.
87 S.-T. Hung, C.-J. Chang, C. C. Chen, C. F. Lo, F. Ren, S. J. Pearton and I. I. Kravchenko, *J. Vac. Sci. Technol., B: Nanotechnol. Microelectron.: Mater., Process., Meas., Phenom.*, 2012, **30**, 041214.
88 P. Offermans, A. Si-Ali, G. Brom-Verheyden, K. Geens, S. Lenci, M. Van Hove, S. Decoutere and R. Van Schaijk, Suspended AlGaN/GaN membrane devices with recessed open gate areas for ultra-low-power air quality monitoring, in *2015 IEEE International Electron Devices Meeting (IEDM)*, 15800977, 2015.
89 N. Sharma, S. Kumar, A. Gupta, S. B. Dolmanan, D. S. K. Patil, S. T. Tan, S. Tripathy and M. Kumar, *Sens. Actuators, A*, 2022, 113647.
90 C. Chang, B. Kang, H. Wang, F. Ren, Y. Wang, S. Pearton, D. Dennis, J. Johnson, P. Rajagopal and J. Roberts, *Appl. Phys. Lett.*, 2008, **92**, 232102.
91 B. Shen, J. Luo, Y. Xie, D. Zhang, P. Fan and A. Zhong, *Appl. Phys. Lett.*, 2019, **115**, 254104.
92 X. Wang, X. Wang, C. Feng, C. Yang, B. Wang, J. Ran, H. Xiao, C. Wang and J. Wang, *Microelectron. J.*, 2008, **39**, 20–23.
93 C.-C. Huang, H.-I. Chen, I.-P. Liu, C.-C. Chen, P.-C. Chou, J.-K. Liou and W.-C. Liu, *Sens. Actuators, B*, 2014, **190**, 913–921.
94 A. Sun, H. Yu, Y. Zhou, Y. Liu, J. Luo, P. Fan and A. Zhong, *Int. J. Hydrogen Energy*, 2022, **47**, 17494–17503.
95 J. Schalwig, G. Müller, M. Eickhoff, O. Ambacher and M. Stutzmann, *Sens. Actuators, B*, 2002, **87**, 425–430.
96 C.-S. Hsu, H.-I. Chen, C.-F. Chang, T.-Y. Chen, C.-C. Huang, P.-C. Chou and W.-C. Liu, *Sens. Actuators, B*, 2012, **165**, 19–23.
97 Z. Guo, L. Wang, Z. Hao and Y. Luo, *Sens. Actuators, B*, 2013, **176**, 241–247.
98 C.-C. Chen, H.-I. Chen, I.-P. Liu, P.-C. Chou, J.-K. Liou, C.-C. Huang and W.-C. Liu, *Sens. Actuators, B*, 2015, **212**, 127–136.
99 H. Kim and S. Jang, *Curr. Appl. Phys.*, 2013, **13**, 1746–1750.
100 G. Chung, T. Vuong and H. Kim, *Results Phys.*, 2019, **12**, 83–84.
101 C.-S. Hsu, K.-W. Lin and W.-C. Liu, *IEEE Sens. J.*, 2013, **13**, 2299–2304.
102 J. Song and W. Lu, AlGaN/GaN Heterostructure Field Effect Transistors for High Temperature Hydrogen Sensing with Enhanced Sensitivity, in *2007 IEEE International Electron Devices Meeting (IEDM)*, 9829228, 2007.
103 C.-S. Hsu, H.-I. Chen, P.-C. Chou, J.-K. Liou, C.-C. Chen, C.-F. Chang and W.-C. Liu, *IEEE Sens. J.*, 2013, **13**, 1787–1793.
104 C.-C. Huang, H.-I. Chen, T.-Y. Chen, C.-S. Hsu, C.-C. Chen, P.-C. Chou, J.-K. Liou and W.-C. Liu, *IEEE Electron Device Lett.*, 2012, **33**, 788–790.
105 S. Nakamura, N. Takahashi and T. Okumura, *Phys. Status Solidi C*, 2009, **6**, S1053–S1055.
106 R. Sokolovskij, J. Zhang, H. Zheng, W. Li, Y. Jiang, G. Yang, H. Yu, P. Sarro and G. Zhang, Recessed gate Pt-AlGaN/GaN HEMT H2 sensor, in *2019 IEEE Sensors*, 19261433, 2019.
107 S.-T. Hung, C.-J. Chang, C.-H. Hsu, B. H. Chu, C. F. Lo, C.-C. Hsu, S. J. Pearton, M. R. Holzworth, P. G. Whiting and N. G. Rudawski, *Int. J. Hydrogen Energy*, 2012, **37**, 13783–13788.
108 J. Song and W. Lu, *IEEE Electron Device Lett.*, 2008, **29**, 1193–1195.
109 J.-H. Choi, H. Kim, H.-K. Sung and H.-Y. Cha, *Sensors*, 2019, **19**, 5549.
110 R. Sokolovskij, J. Zhang, H. Zheng, W. Li, Y. Jiang, G. Yang, H. Yu, P. M. Sarro and G. Zhang, *IEEE Sens. J.*, 2020, **20**, 8947–8955.
111 H. O. Chahdi, O. Helli, N.-E. Bourzgui, L. Breuil, D. Danovitch, P. L. Voss, S. Sundaram, V. Aubry, Y. Halfaya and A. Ougazzaden, Sensors based on AlGaN/GaN HEMT for fast H2 and O2 detection and measurement at high temperature, in *2019 IEEE Sensors*, 19261426, 2019.
112 R. Sokolovskij, J. Zhang, Y. Jiang, G. Chen, G. Q. Zhang and H. Yu, AlGaN/GaN HEMT micro-sensor technology for gas sensing applications, in *2018 14th IEEE International Conference on Solid-State and Integrated Circuit Technology (ICSICT)*, 18321320, 2018.
113 R. Sokolovskij, E. Iervolino, C. Zhao, F. Santagata, F. Wang, H. Yu, P. M. Sarro and G. Q. Zhang, Multidisciplinary Digital Publishing Institute Proceedings, 2017, vol. 1, p. 463.
114 W.-C. Chen, J.-S. Niu, I.-P. Liu, B.-Y. Liu, S.-Y. Cheng, K.-W. Lin and W.-C. Liu, *IEEE Trans. Electron Devices*, 2020, **68**, 761–768.
115 Y. Halfaya, C. Bishop, A. Soltani, S. Sundaram, V. Aubry, P. L. Voss, J.-P. Salvestrini and A. Ougazzaden, *Sensors*, 2016, **16**, 273.
116 A. Ahaitouf, Y. Halfaya, S. Sundaram, S. Gautier, P. Voss, J. P. Salvestrini and A. Ougazzaden, *Eng. Proc.*, 2020, **2**, 58.
117 R. Vitushinsky, M. Crego-Calama, S. Brongersma and P. Offermans, *Appl. Phys. Lett.*, 2013, **102**, 172101.
118 P. Offermans, R. Vitushinsky, M. Crego-Calama and S. H. Brongersma, *Procedia Eng.*, 2011, **25**, 1417–1420.

119 V. C. Nguyen, H.-Y. Cha and H. Kim, *J. Semicond. Technol. Sci.*, 2021, **21**(6), 412–417.
120 M. Lim, S. Mills, B. Lee and V. Misra, *ECS J. Solid State Sci. Technol.*, 2015, **4**, S3034.
121 V. C. Nguyen, K. Kim and H. Kim, *Micromachines*, 2021, **12**, 400.
122 A. Ranjan, M. Agrawal, K. Radhakrishnan and N. Dharmarasu, *Jpn. J. Appl. Phys.*, 2019, **58**, SCCD23.
123 P. Offermans and R. Vitushinsky, *IEEE Sens. J.*, 2013, **13**, 2823–2827.
124 T. Ayari, C. Bishop, M. B. Jordan, S. Sundaram, X. Li, S. Alam, Y. ElGmili, G. Patriarche, P. L. Voss and J. P. Salvestrini, *Sci. Rep.*, 2017, **7**, 1–8.
125 M. A. H. Khan, B. Thomson, R. Debnath, A. Rani, A. Motayed and M. V. Rao, *Nanotechnology*, 2020, **31**, 155504.
126 K. H. Baik and S. Jang, *Sens. Mater.*, 2020, **32**, 2569–2576.
127 C.-F. Lo, B. Chu, S. Pearton, A. Dabiran, P. Chow, S. Dore, S. Hung, C. Chen and F. Ren, *Appl. Phys. Lett.*, 2011, **99**, 142107.
128 C.-F. Lo, L. Liu, B.-H. Chu, F. Ren, S. J. Pearton, S. Doré, C.-H. Hsu, J. Kim, A. M. Dabiran and P. P. Chow, *J. Vac. Sci. Technol., B: Nanotechnol. Microelectron.: Mater., Process., Meas., Phenom.*, 2012, **30**, 010606.
129 M. Mishra, N. K. Bhalla, A. Dash and G. Gupta, *Appl. Surf. Sci.*, 2019, **481**, 379–384.
130 B. Kang, S. Kim, F. Ren, K. Ip, Y. Heo, B. Gila, C. Abernathy, D. Norton and S. Pearton, *J. Electrochem. Soc.*, 2004, **151**, G468.
131 I.-P. Liu, C.-H. Chang, Y.-M. Huang and K.-W. Lin, *Int. J. Hydrogen Energy*, 2019, **44**, 5748–5754.
132 C.-C. Chen, H.-I. Chen, I.-P. Liu, H.-Y. Liu, P.-C. Chou, J.-K. Liou and W.-C. Liu, *Sens. Actuators, B*, 2015, **211**, 303–309.
133 H.-I. Chen, K.-C. Chuang, C.-H. Chang, W.-C. Chen, I.-P. Liu and W.-C. Liu, *Sens. Actuators, B*, 2017, **246**, 408–414.
134 T.-H. Tsai, J.-R. Huang, K.-W. Lin, W.-C. Hsu, H.-I. Chen and W.-C. Liu, *Sens. Actuators, B*, 2008, **129**, 292–302.
135 I. Rýger, G. Vanko, P. Kunzo, T. Lalinský, M. Vallo, A. Plecenik, L. Satrapinský and T. Plecenik, *Procedia Eng.*, 2012, **47**, 518–521.
136 H.-I. Chen, C.-H. Chang, H.-H. Lu, I.-P. Liu, W.-C. Chen, B.-Y. Ke and W.-C. Liu, *Sens. Actuators, B*, 2018, **262**, 852–859.
137 M. Miyoshi, S. Fujita and T. Egawa, *J. Vac. Sci. Technol., B: Nanotechnol. Microelectron.: Mater., Process., Meas., Phenom.*, 2015, **33**, 013001.
138 B.-Y. Liu and W.-C. Liu, *IEEE Trans. Electron Devices*, 2020, **67**, 2566–2572.
139 J. Schalwig, G. Müller, U. Karrer, M. Eickhoff, O. Ambacher, M. Stutzmann, L. Görgens and G. Dollinger, *Appl. Phys. Lett.*, 2002, **80**, 1222–1224.
140 J. Ahn, D. Kim, K.-H. Park, G. Yoo and J. Heo, *IEEE Trans. Electron Devices*, 2021, **68**, 1255–1261.
141 I.-P. Liu, C.-H. Chang and B.-Y. Ke, *ACS Appl. Electron. Mater.*, 2019, **1**, 1474–1481.
142 C.-H. Chang, K.-W. Lin, H.-H. Lu, R.-C. Liu and W.-C. Liu, *Int. J. Hydrogen Energy*, 2018, **43**, 19816–19824.
143 I.-P. Liu, C.-H. Chang, B.-Y. Ke and K.-W. Lin, *Int. J. Hydrogen Energy*, 2019, **44**, 32351–32361.
144 T.-H. Tsai, H.-I. Chen, K.-W. Lin, Y.-W. Kuo, C.-F. Chang, C.-W. Hung, L.-Y. Chen, T.-P. Chen, Y.-C. Liu and W.-C. Liu, *Sens. Actuators, B*, 2009, **136**, 338–343.
145 I.-P. Liu, C.-H. Chang, H.-H. Lu and K.-W. Lin, *Sens. Actuators, B*, 2019, **296**, 126599.
146 W.-C. Chen, J.-S. Niu, I.-P. Liu, H.-Y. Chen, S.-Y. Cheng, K.-W. Lin and W.-C. Liu, *Sens. Actuators, B*, 2021, **330**, 129339.
147 B.-Y. Ke and W.-C. Liu, *IEEE Trans. Electron Devices*, 2018, **65**, 4577–4584.
148 H.-Y. Chen and W.-C. Liu, *IEEE Trans. Electron Devices*, 2019, **66**, 3144–3150.
149 B. Kang, R. Mehandru, S. Kim, F. Ren, R. Fitch, J. Gillespie, N. Moser, G. Jessen, T. Jenkins and R. Dettmer, *Phys. Status Solidi C*, 2005, **2**, 2672–2675.
150 I.-P. Liu, C.-H. Chang, Y.-M. Huang and K.-W. Lin, *IEEE J. Electron Devices Soc.*, 2019, **7**, 476–482.
151 O. Weidemann, M. Hermann, G. Steinhoff, H. Wingbrant, A. Lloyd Spetz, M. Stutzmann and M. Eickhoff, *Appl. Phys. Lett.*, 2003, **83**, 773–775.
152 M. Johansson, I. Lundström and L.-G. Ekedahl, *J. Appl. Phys.*, 1998, **84**, 44–51.
153 C. Christofides and A. Mandelis, *J. Appl. Phys.*, 1990, **68**, R1–R30.
154 P. Atkins and J. De Paula, *Physical chemistry*, Macmillan, 2002.
155 K. Brudzewski and J. Ulaczyk, *Sens. Actuators, B*, 2009, **140**, 43–50.
156 L. Zhu, H. Jia, Y. Chen, Q. Wang, M. Li, D. Huang and Y. Bai, *Sensors*, 2019, **19**, 3417.
157 C. Distante, M. Leo, P. Siciliano and K. C. Persaud, *Sens. Actuators, B*, 2002, **87**, 274–288.
158 E. Llobet, J. Brezmes, X. Vilanova, J. E. Sueiras and X. Correig, *Sens. Actuators, B*, 1997, **41**, 13–21.
159 N. Paulsson, E. Larsson and F. Winquist, *Sens. Actuators, A*, 2000, **84**, 187–197.
160 K. Yan and D. Zhang, Blood glucose prediction by breath analysis system with feature selection and model fusion, in *2014 36th annual international conference of the IEEE engineering in medicine and biology society*, 14734710, 2014.
161 J. H. Cho and P. U. Kurup, *Sens. Actuators, B*, 2011, **160**, 542–548.
162 S. Lekha and M. Suchetha, *IEEE J. Biomed. Health Inform.*, 2017, **22**, 1630–1636.
163 W. Zhang, L. Wang, J. Chen, X. Bi, C. Chen, J. Zhang and V. Hans, *IEEE Sens. J.*, 2021, **21**, 18459–18468.
164 W. Zhang, H. Xiang, Y. Wang, X. Bi, Y. Zhang, P. Zhang, J. Chen, L. Wang and Y. Zheng, *IEEE Sens. J.*, 2022, **22**, 14717–14726.
165 T. Wang, H. M. Huang, X. X. Wang and X. Guo, *InfoMat*, 2021, **3**, 804–813.
166 J. K. Han, M. Kang, J. Jeong, I. Cho, J. M. Yu, K. J. Yoon, I. Park and Y. K. Choi, *Adv. Sci.*, 2022, 2106017.
167 C. Ban, X. Min, J. Xu, F. Xiu, Y. Nie, Y. Hu, H. Zhang, M. Eginligil, J. Liu and W. Zhang, *Adv. Mater. Technol.*, 2021, **6**, 2100366.

168 Z. Gao, S. Chen, R. Li, Z. Lou, W. Han, K. Jiang, F. Qu and G. Shen, *Nano Energy*, 2021, **86**, 106078.
169 M. A. H. Khan, M. V. Rao and Q. Li, *Sensors*, 2019, **19**, 905.
170 P. Ramaswamy, IoT smart parking system for reducing green house gas emission, in *2016 International Conference on Recent Trends in Information Technology (ICRTIT)*, 16320683, 2016.
171 J.-H. Suh, I. Cho, K. Kang, S.-J. Kweon, M. Lee, H.-J. Yoo and I. Park, *Sens. Actuators, B*, 2018, **265**, 660–667.
172 G. Alcantara and C. Andrade, A short review of gas sensors based on interdigital electrode, in *2015 12th IEEE International Conference on Electronic Measurement & Instruments (ICEMI)*, 2015.